Università degli Studi di Napoli "Federico II"

SCUOLA POLITECNICA E DELLE SCIENZE DI BASE

DIPARTIMENTO DI INGEGNERIA INDUSTRIALE

CORSO DI LAUREA IN INGEGNERIA AEROSPAZIALE

CLASSE DELLE LAUREE IN INGEGNERIA INDUSTRIALE (L-9)

Elaborato di laurea in Meccanica del Volo
Geometric modelling, performance and static stability analysis of the PD-1 UAV with OpenVSP

Relatore:
Prof. Danilo Ciliberti

Candidato:
Stefano Barrella
Matr. N35003556

ANNO ACCADEMICO 2021 – 2022

Alla mia famiglia,
Ai miei amici,
Alla vita vissuta.

"lo studio non deve essere l'unica ragione alla vostra vita, se così fosse sareste degli sbandati, lo studio e il pezzo più importante di questa fase della vostra vita ma date spazio ad altre passioni. Un ingegnere davvero equilibrato è un ingegnere che ama lo sport, la musica e frequentare gli amici quindi, no secchioni, studiate, studiate molto ma con attenzione."

Prof. Luigi Carrino

Abstract

The following thesis project's target is the geometric modelling of the unmanned Ukrainian vehicle PD-1 which I made using the open-source platform OPENVSP. Stability and control analysis can be performed on the geometric model exploiting one of the tools that OPENVSP provides. The presented aerodynamic analysis has been realised with the VSPAERO tool. VSPAERO lets the user choose between two methods to compute aerodynamic evaluations: vortex lattice method (VLM) and panel method. In this thesis project I used VLM. Vortex lattice method is a numerical method exploited for aircraft aerodynamic analysis that is widely and particularly used in first steps design. The results that the VLM worked out have been collected and commented in order to describe a complete scenario that concerns static stability (and control. Subsequently the thesis project is about how the propulsive effects could alter the previous results. In conclusion the work shows some flight performance of the UAV computed using MATLAB scripts proposed by the thesis supervisor.

Sommario

Il fine del seguente lavoro di tesi consiste nella modellazione geometrica del velivolo a pilotaggio remoto ucraino PD-1 tramite l'utilizzo della piattaforma open source OPENVSP. Sul modello geometrico realizzato sono state svolte diverse analisi riguardanti stabilità e controllo, le quali possono essere realizzate attraverso uno dei diversi tool che OPENVSP ha integrato al suo interno. Le analisi aerodinamiche presentate sono state eseguite attraverso il tool VSPAERO, quest'ultimo dispone di due metodi per lo svolgimento delle analisi aerodinamiche: il metodo dei panelli e il metodo vortex lattice. L'utente può scegliere uno dei due metodi e in questo lavoro di tesi è stato usato quest'ultimo. Il vortex lattice method (VLM) è un metodo numerico usato per l'analisi aerodinamica dei velivoli ampiamente adoperato soprattutto nelle prime fasi di design. I risultati ottenuti dallo studio attraverso il VLM sono stati raccolti e commentati in modo da fornire un quadro completo per quello che riguarda la stabilità statica, dinamica e il controllo. Successivamente il lavoro ha riguardato la valutazione degli effetti propulsivi sui calcoli precedentemente svolti per poi concludersi con il calcolo di alcune prestazioni del velivolo utilizzando script MATLAB proposti dal relatore.

Table of contents

List of figures

List of tables

1. Introduction

1.1 Objectives

The aim of this work consists in realising a geometric model of the PD1-UAV and using it for aerodynamic studies. The results obtained from this work are a preliminary data set that should be tested in the wind tunnel. In fact, VSPAERO and VLM present their limits thus they can be used only as first evaluation of aerodynamic performance, stability and control. The data obtained from VSPAERO was processed in Microsoft excel to show characteristics curve of the UAV and other useful data. The latter contains lift, polar drag, momentum coefficients and stability derivatives. This thesis wants to value even the performance of an inverted V tail and propulsive effects of a trusting propeller.

1.2 Layout of the work

Chapter 1: This chapter presents the PD1 and shows stability and control basis for UAVs.

Chapter 2: This chapter describes vortex lattice method, the numerical method exploited by VSPAERO to compute its analysis.

Chapter 3: This Chapter introduce OpenVSP modeller and show how the PD-1 model has been created.

Chapter 4: In this chapter will be discussed the results output of longitudinal aerodynamics analysis.

Chapter 5: In this chapter will be discussed the results output of lateral and directional analysis.

Chapter 6: This chapter deal about possible propulsive effects on longitudinal aerodynamics curves.

Chapter 7: In this chapter will be presented some performance of the PD-1 calculated with MATLAB scripts given by the thesis supervisor.

1.3 UAV PD-1

The People's Drone PD-1 unmanned aerial system (UAS) is designed and manufactured by UkrSpecSystems, a UAS producer based in Ukraine. This UAV is a close-range UAV which means that it is used for military and civilian purposes that request ranges of about 100 km. Specifically the PD-1 is designed for military and civilian missions such as aerial surveillance, observation, monitoring, intelligence, reconnaissance, and photomapping.

Figure 1.1 The PD-1 unmanned air vehicle.

The aircraft configuration is a twin-boom arrangement with the engine mounted as a pusher system just aft of the wing. This configuration is widely used for UAV's because it frees the front fuselage for payload installation and it also provides protection for the engine and propeller. The PD-1's wing presents winglets that are used with the aim of reducing the wingtip vortices, downwash and induced drag. It also presents control surfaces (ailerons) and high lift devices (flaps). The tail plane of this aircraft is its uniqueness in fact it is an inverted V-tail with a dihedral of about -35°. This huge dihedral led designers to use *ruddervators* as control surfaces. In V-tail UAV (or in this case inverted V-tail UAV), the movable control surfaces of the tail are called *ruddervators*. These function as rudders when moving differentially and as elevators when moving together.

1.4 UAV flight stability and control

1.4.1 Flight stability and control surfaces

Stability is defined as the tendency of the UAV to return to a condition of equilibrium when subjected to a disturbance in flight, particularly static stability is the initial response of the aircraft to regain equilibrium upon a disturbance and it can be positive negative or neutral [1]. The aircraft's longitudinal static stability depends on the centre of gravity (CG) location. It is neutral if the CG is in the aircraft's neutral point (NP), it is positive if it is placed ahead of the neutral point and it is negative when it is moved aft. This criterion can be easily redefined presenting the stability margin SM as the distance between the CG and NP in body axes. A large SM implies a very stable but not particularly maneuverable aircraft. Highly maneuverable UAVs have a short positive SM. Conventional aircraft control surfaces produce the moments that cause rotations in pitch, yaw and roll in order to control the aircraft attitude. Often in UAVs, the function of two control surfaces is combined in a single surface. Other than *ruddervators* (that are present in the PD-1) there are elevons and flaperons.

1.4.2 Stability derivatives

Moments on a UAV are created by the aerodynamic load distribution and the thrust force non acting through the CG. Aerodynamic moments are expressed in terms of the dimensionless coefficients for pitching moment (C_M), rolling moment (C_R) and yawing moment (C_N). The values of C_M, C_R and C_N depend on the angle of attack (α), Reynolds number (Re), Mach number (M) and sideslip angle (β). A necessary condition for longitudinal static stability of the UAV is that the pitching moment curve has a negative slope through the equilibrium point. The slope must be negative for lateral static stability and positive for directional static stability (all the derivatives are referred to BRF)[1].
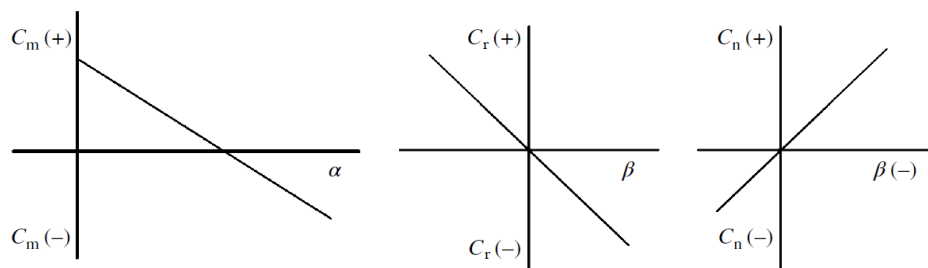
Figure 1.2 Stability conditions

13

2. Vortex lattice Method

VSPAERO let the user choose between two methods, the first is the Vortex Lattice Method (VLM) and the second one is Panel Method; In this chapter the focus will be on the first of the two methods listed because the following results of this work have been obtained using VLM.

2.1 Aerodynamic background

2.1.1 Flow description

VLM is a widely used computational fluid dynamics method that is reliable to estimate aerodynamic load distribution and so forces and momentum acting on the aircraft in initial stages of aircraft design. The VLM works under the following assumptions:

- The flow field is incompressible, inviscid and irrotational.
- The lifting surface is thin and that results in a neglected influence of thickness on aerodynamic forces.
- Small angle of attack and sideslip.

Under these assumptions, it is possible to express:

$$\nabla \times V = 0 \tag{2.1}$$

$$\nabla \cdot V = 0 \tag{2.2}$$

Defined φ as a scalar function, following the vector identity it follows that:

$$\nabla \times (\nabla \varphi) = 0 \tag{2.3}$$

Combining equation (2.2) and equation (2.3), gives:

$$V = \nabla \varphi \tag{2.4}$$

Equations (2.4) states that under the assumptions made, it is possible to define a scalar function φ such that the velocity is given by the gradient of φ and its name is velocity potential.

By combining the equations (2.4) and (2.2) the result is the Prandtl-Glauert equation, which governs irrotational and incompressible flow. The Prandtl-Glauert equation is a linear equation, and this means that a complicated solution can be obtained by adding together elementary solutions. Particularly, the VLM models the lifting surfaces, such as a wing, of an aircraft as an infinitely thin sheet of discrete vortices to compute lift and induced drag. Since the VLM is based on potential flow theory, it is not possible to evaluate viscous drag. VSPAERO can only approximate viscous drag and CD0, but it can compute only induced drag starting from the production of lift.

2.1.2 Boundary conditions

VLM exploits thin airfoil boundary condition. Under this hypothesis pressure coefficients can be linearized, and it is possible to see how thickness effects can be neglected. Furthermore, considering symmetric airfoils also the camber effects can be neglected. Considering these two statements, boundary conditions can easily be applied to a flat surface deflected with an angle of attack α (Figure 2.1).
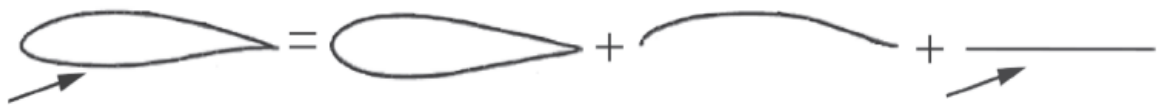
Figure 2.1 Decomposition of a profile under thin airfoil hypothesis

The boundary condition states that the normal flow across the wing solid surface is zero:

$$\nabla(\varphi + \varphi_\infty) = 0 \tag{2.5}$$

Which means that the sum of the normal velocity component induced by the wing's bound vortices w_b, by the wake w_i and by the free-stream velocity V_∞ will be zero:

$$w_b + w_i + V_\infty \cdot \alpha = 0 \tag{2.6}$$

2.1.3 Biot-Savart law and Kutta-Jukowsky theorem

As shown, the line vortex is a possible solution for Laplace's equation. The vortex flow is shown in Figure 2.1. These vortices induce an increment of velocity dV at a point P given by the Biot-Savart law (equation 2.7). It states that that the induced velocity dV at a point P due to a segment of a vortex filament dl a point q is directly proportional to the vortex strength Γ and inversely proportional to the square of the distance r_{Pq}.

$$dV_P = \frac{\Gamma}{4\pi} \cdot \frac{dl \times r_{Pq}}{|r_{Pq}|^3} \qquad (2.7)$$
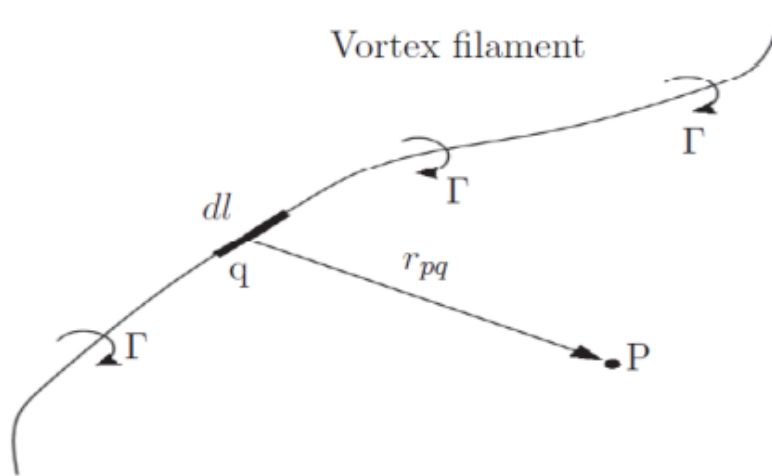
Figure 2.2 Line vortex

The VLM uses a special form of vortex, specifically this method is an extension of Prandtl lifting line theory, where the wing of an aircraft is modelled as an infinite number of horseshoe vortices instead of only one horseshoe vortex per wing. Horseshoe vortices consist of four vortex filaments: two trailing segments *ab* and *cd* of the vortex are placed parallel to the direction of the free stream velocity and start at infinity. The other two segments *bc* and *ad* are finite. Normally, the effect of *ad* is neglected owing to its infinite distance. So, in practice, the horseshoe vortex is made up by only three parts. Referring to the Biot-Savart law the induced velocity at a point can be expressed in general as:

$$V_P = V_{bc} + V_{b\infty} + V_{c\infty} \qquad (2.8)$$

16

As mentioned, the horseshoe vortex is going to represent the lifting surface. To evaluate V_P is essential to establish the location of P (control point) and the location of the vortex. The vortex is located at the ¼ chord point, and the control point is located at the ¾ chord point. The rule was discovered by Pistolesi and has been proven to be sufficiently accurate in practice.

As said a wing is divided into a finite number of panels (chordwise and spanwise) and on each of those a horseshoe vortex is located. Each of them has its own circulation and induces a velocity in its control point. In order to evaluate the total aerodynamic force, the contribution of all panels must be summed (Figure 2.3).
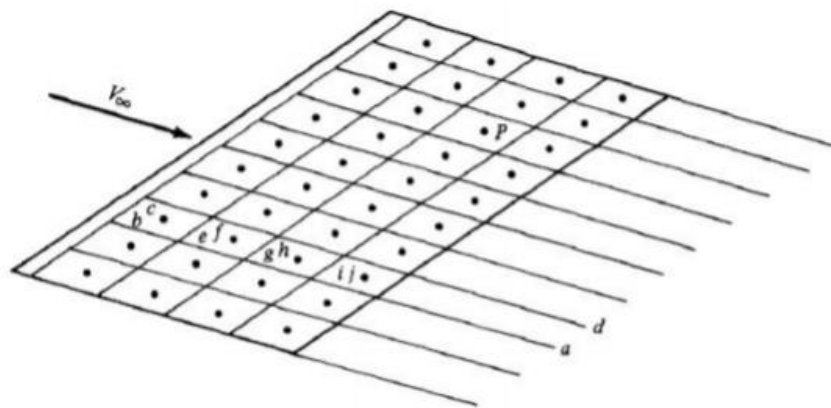
Figure 2.3-vortex lattice system

2.2 VLM

The strength of the horseshoe vortex Γ is computed knowing that vector sum of vortex induced velocity and the freestream contribution at each control point satisfies the boundary condition of a zero normal velocity component. In fact, imposing the boundary condition, Γ is the only unknown term (it is present in the induced velocity according to Biot-Savart law). After that Γ has been computed, it can be used in the Kutta-Jukowski theorem to evaluate load distribution and then lift. Using these parameters also induced drag and momentum coefficients can be evaluated.

VSPAERO do not use properly VLM in its strict definition but it uses a mean surface approach. This means that camber effects of wings and fuselages (contrary to thickness) are considered in the analysis. Specifically, wings have the same camber of the airfoil selected, while fuselages are replaced with two mean surfaces arranged to make a cross.

3. Geometric Modelling

3.1 OpenVSP

OpenVSP is an open-source parametric aircraft geometry, developed originally by NASA. It gives the user the possibility to create three-dimensional models of aircraft and to do engineering and aerodynamic analysis on those models. OpenVSP lets the user choose between different integrated tools to do structural or aerodynamic tests. As mentioned, VSPAERO is the tool used in the following chapters.

3.1.1 Graphical interface

When OpenVSP is launched, a large initial panel appears and a geometry browser next to it. Using the geometry browser, the user can add all the individual elements of an aircraft. In Figure 3.1 is represented how the geometry browser looks like. Clicking on a component, it will be selected, and a geometry window will open. That window permits the user to modify the parameters of the selected component (Figure 3.2).
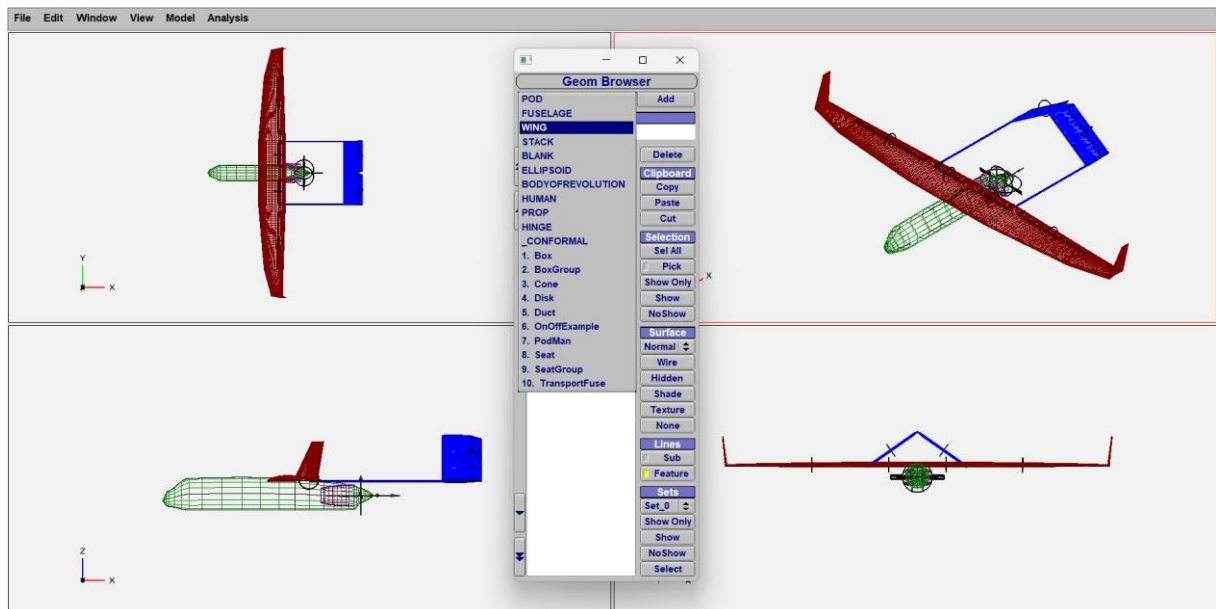
Figure 3.1 OpenVSP graphical interface and geometry browser
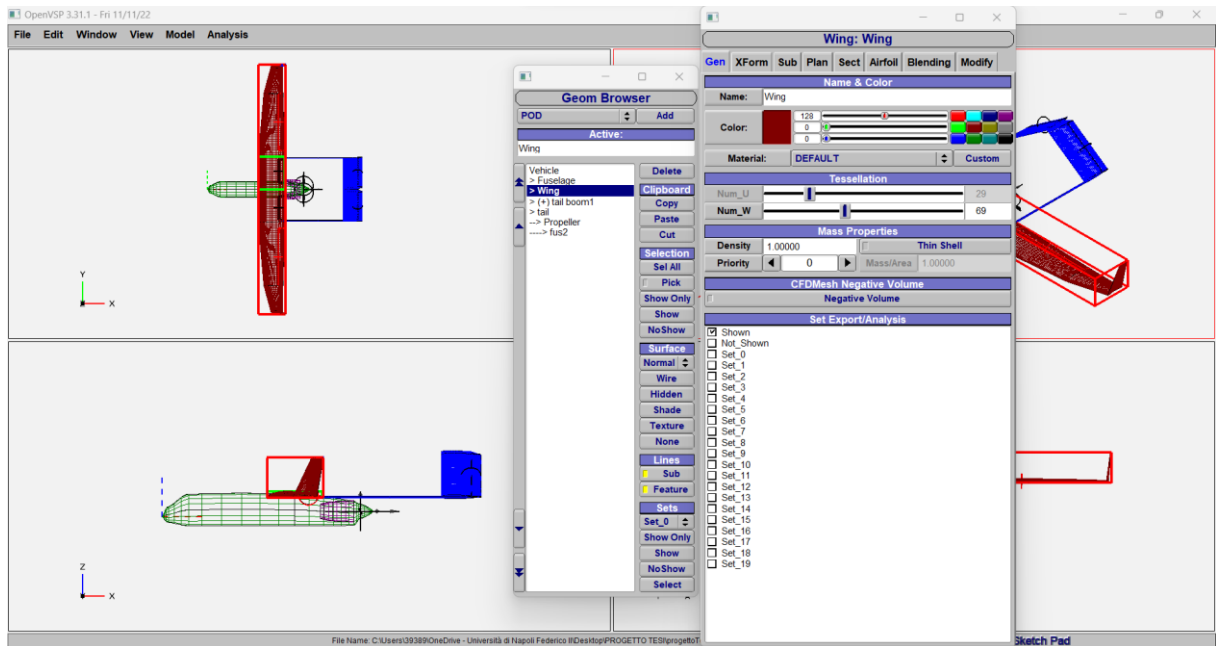
Figure 3.2 OpenVSP workspace with geometry browser and geometry window opened.

3.2 General aspects of the model

PD-1's measures used to realize this model are contained in the drawing in Figure 3.3. The measures not indicated in the drawing have been estimated using the measuring tool of Adobe Acrobat Reader and they have been expressed in feet on OpenVSP. As regards airfoils, their parameters and performance have been obtained from the website www.airfoiltools.com.
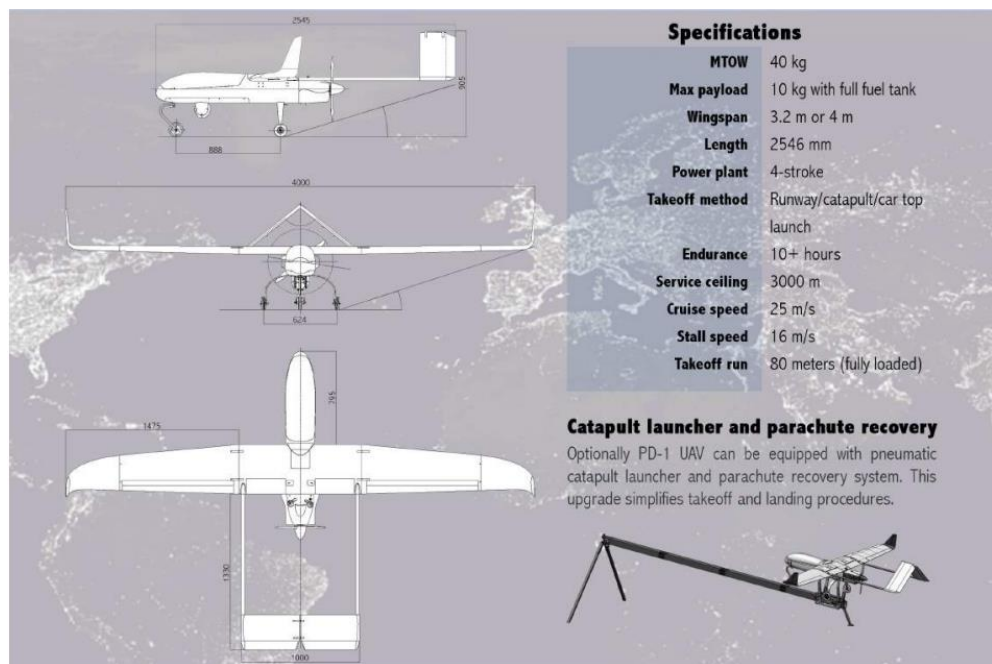
Figure 3.3 PD-1 Drawing taken from the UkrSpecSystem specification list.

19

The work does not present the calculation for the most suitable spanwise and chordwise refinements that define the grid where VLM works (num_U and num _W). In fact, U and W for wing and tailplane have been selected exploiting previous works evaluations [5]. Fuselages refinements does not affect considerably aerodynamic analysis, thus it is not necessary to calculate the most suitable U and W. Owing to this, the grid chosen is less dense to lower the computational cost.
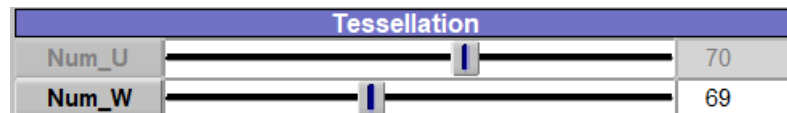
Figure 3.4 Wing and tailplane refinements
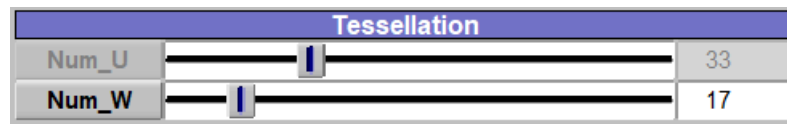
Figure 3.5 Fuselage refinements

3.3 PD-1 modelling

This section shows how PD-1's single elements have been modelled and the parameters used to do it.
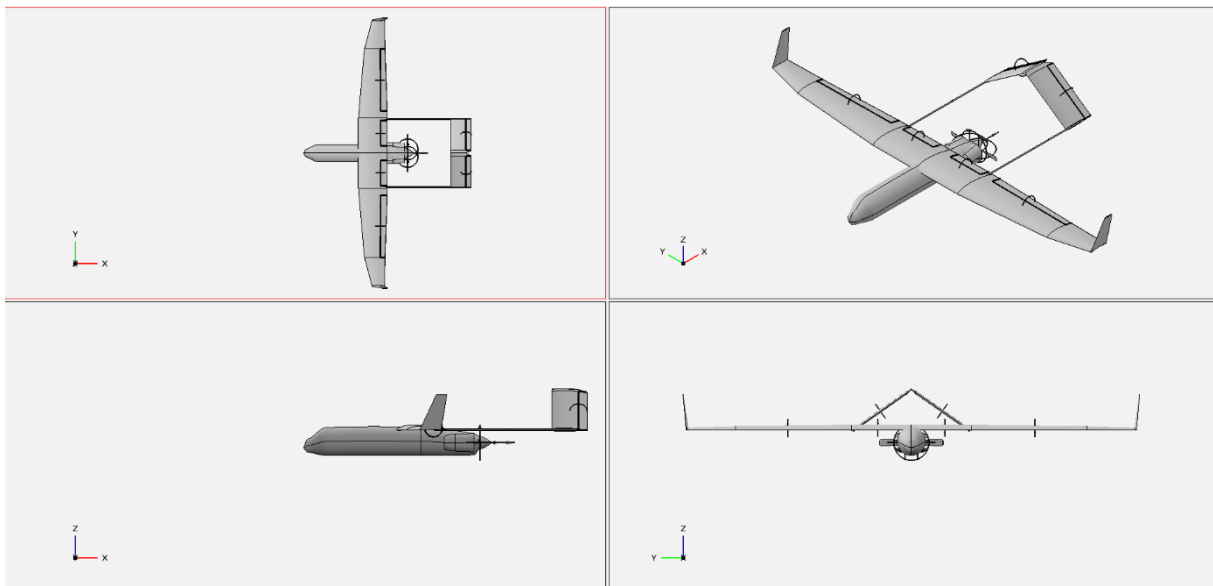
Figure 3.6 PD-1 complete model in shade view

3.3.1 Fuselage
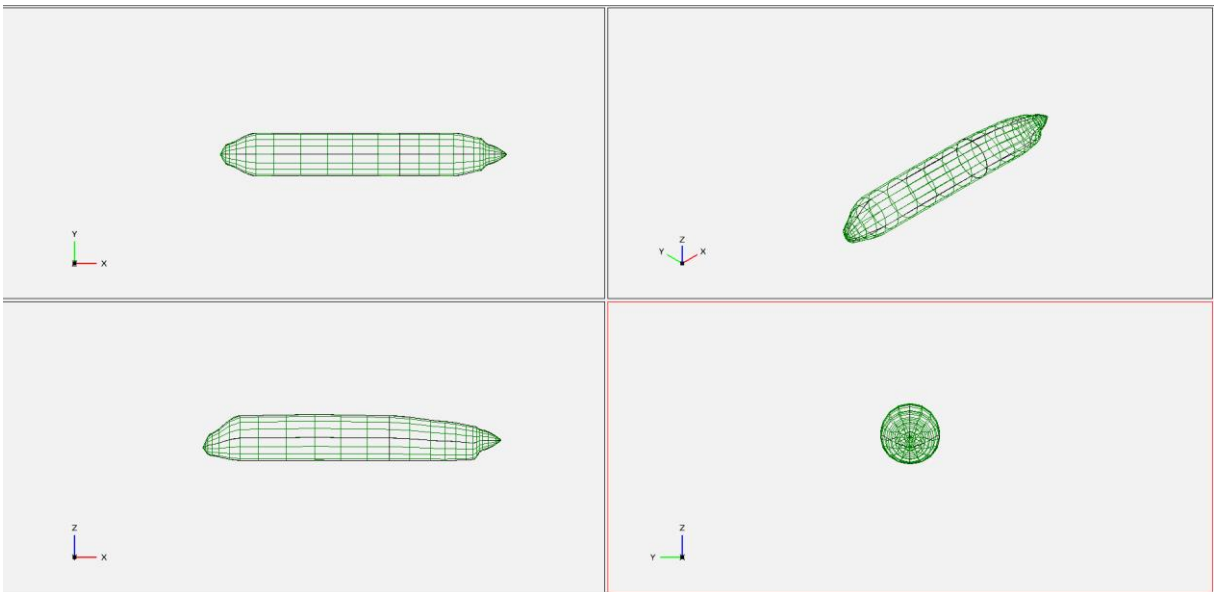
Figure 3.7 Fuselage seen from four point of view.
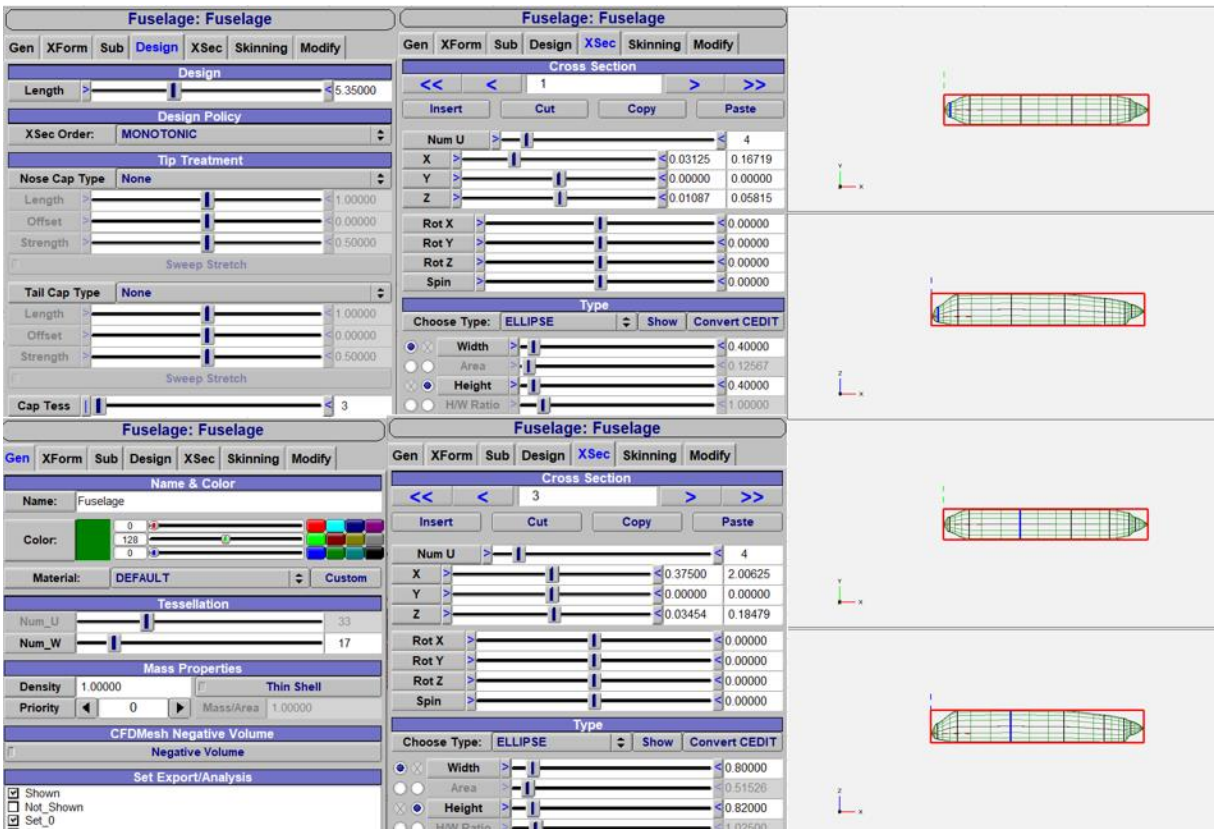
Figure 3.8 Fuselage's general parameters and example of two cross sections

3.3.2 Wing
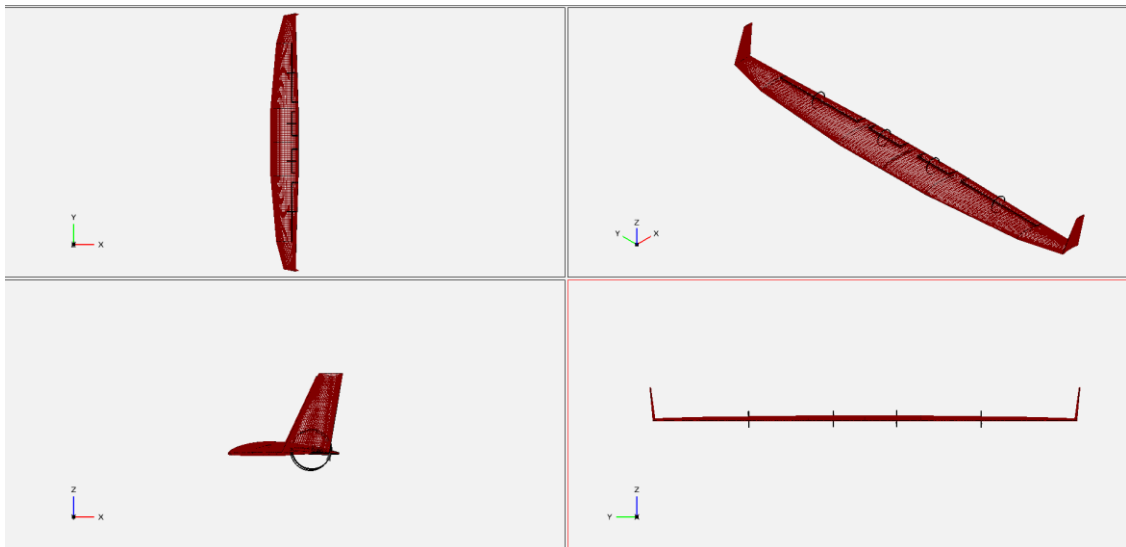
Figure 3.9 Wing seen from four point of view.
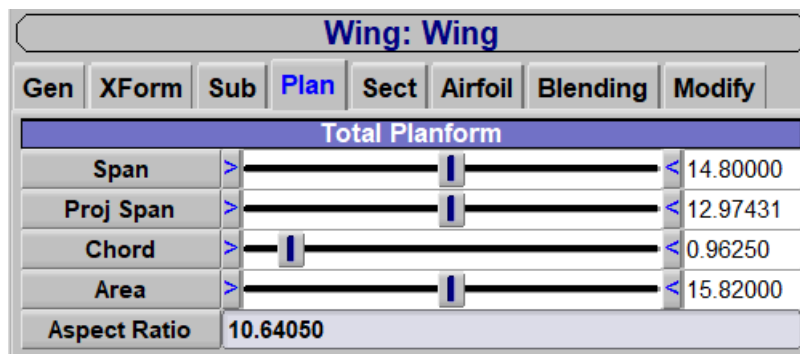
Figure 3.10 Wing general parameters.

Note that "Chord" is the medium chord, instead the local chords will be shown for each section subsequently (Figure 3.11 to Figure 3.14) .

Span, chord and area will be reference lengths and area in VSPAERO analysis as long as the user does not change the settings.

The following pictures present all the four sections of the wing and its parameters including the winglets.
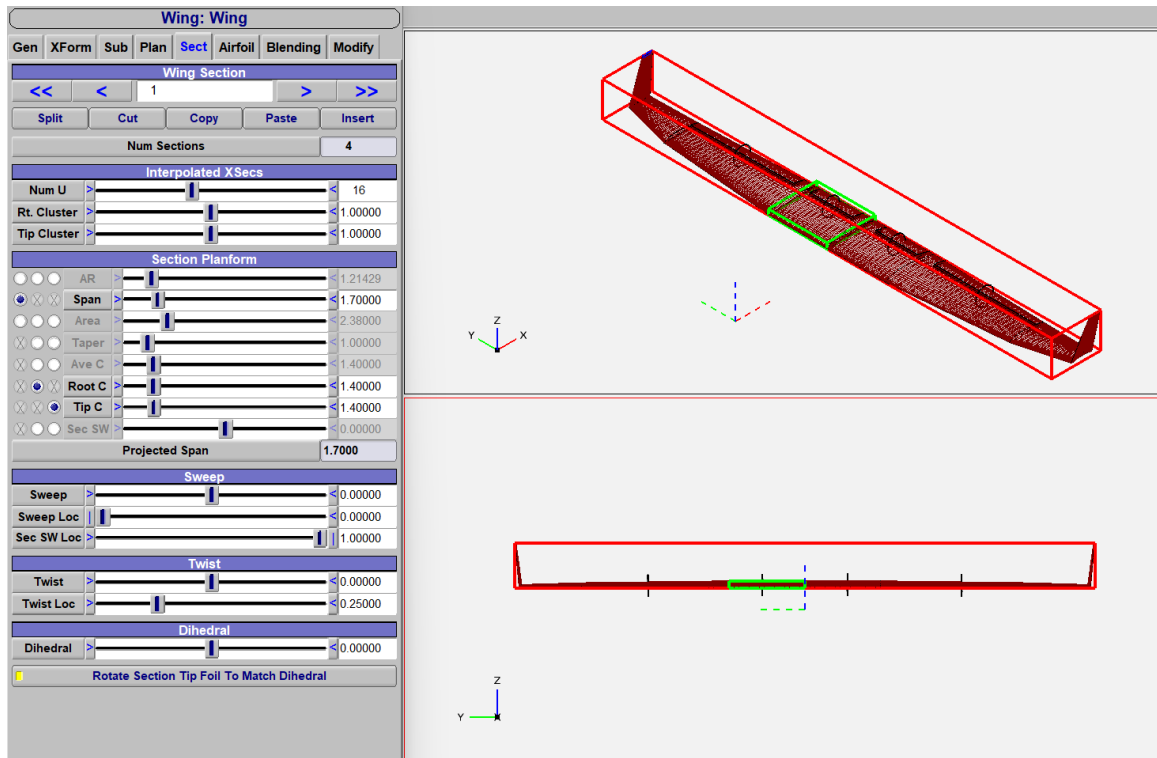
Figure 3.11 Wing section 1
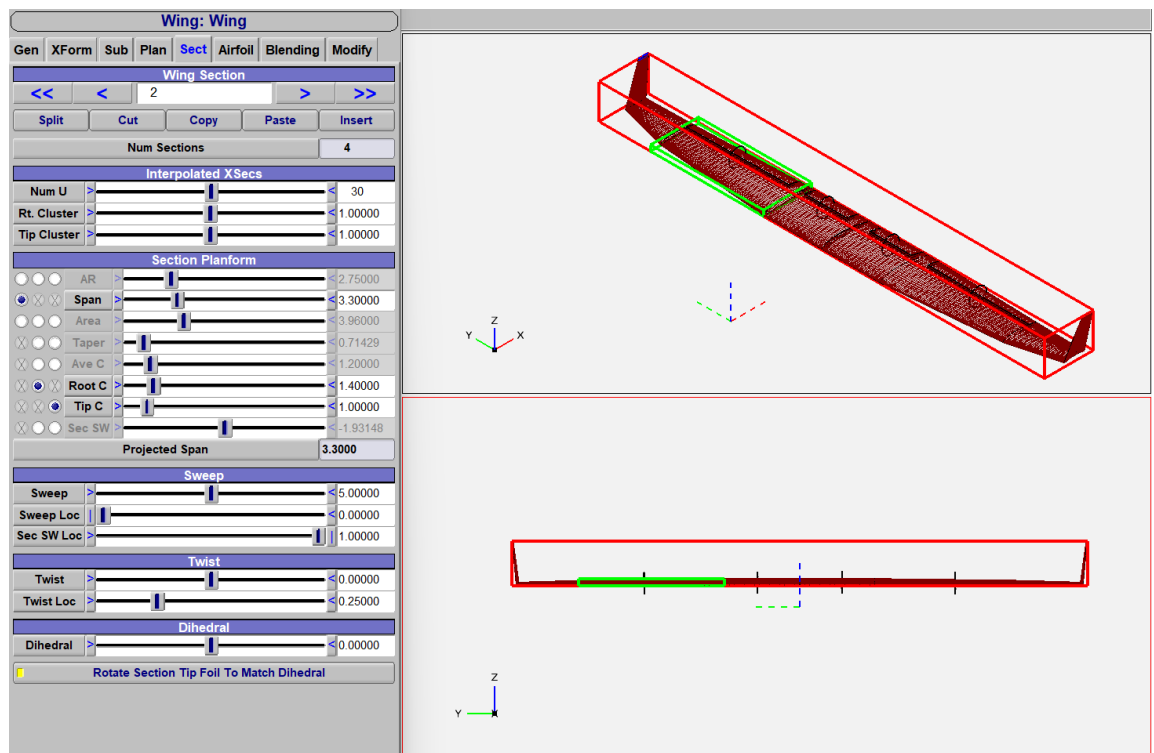
Figure 3.12 Wing section 2
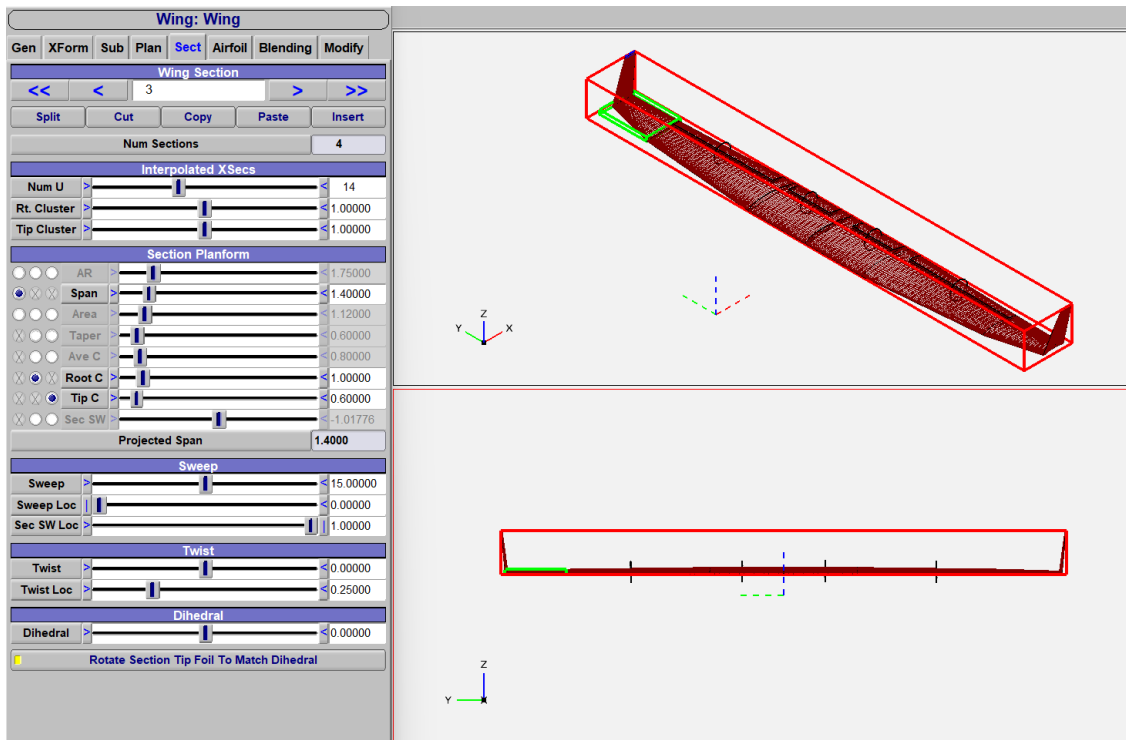
Figure 3.13 Wing section 3
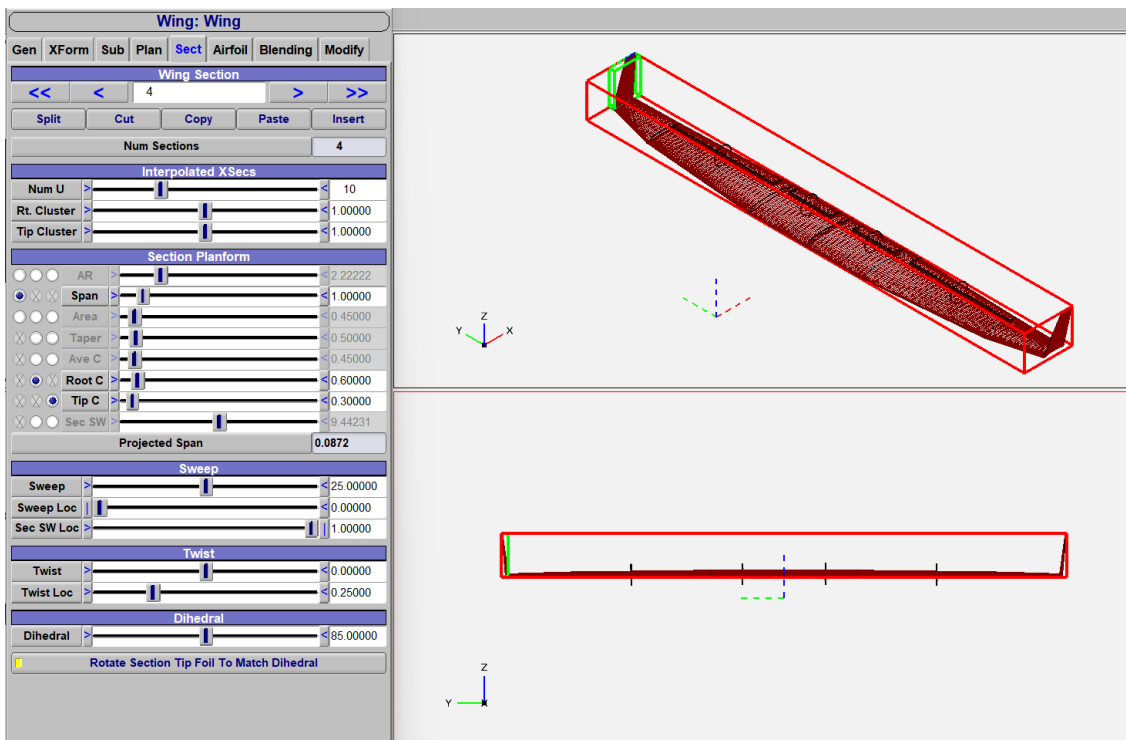
Figure 3.14 Winglets

Note that the setting "rotate section tip foil to match dihedral" is on. This setting is particularly important when huge dihedral angles are present as the case of winglets.

As regards airfoils, the wing is modelled with a NACA6409 (Figure 3.15) owing to its exceptional performance at low Reynolds number regime (PD-1 flights at Re of about 500000). For example, Figure 3.16 compares NACA6409's lift coefficient curve with the symmetric airfoil NACA0012 at Re=500000 (comparison made used www.airfoiltools.com). Note how C_L is higher for each angle of attack and, that α_{0L} is around -5° for NACA6409 rather than 0°. For the winglet has been selected a symmetric airfoil NACA0010 (Figure 3.17).

NACA6409 9% (n6409-il)
NACA6409 9% - NACA 6409
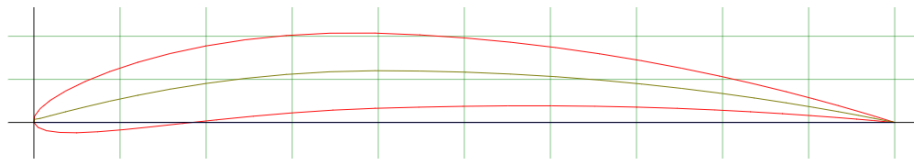
Figure 3.15 Airfoil NACA6409 taken from www.airfoiltools.com.
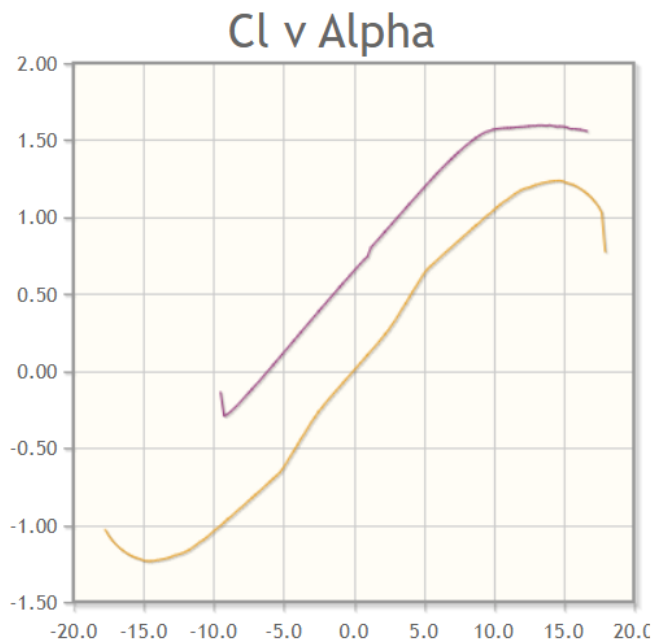
Figure 3.16 C_L curves at Re=500000 of NACA6409 (in purple) and NACA0012 (in yellow). Chart taken from www.airfoilttols.com.

NACA 0010 (naca0010-il)
NACA 0010 - NACA 0010 airfoil
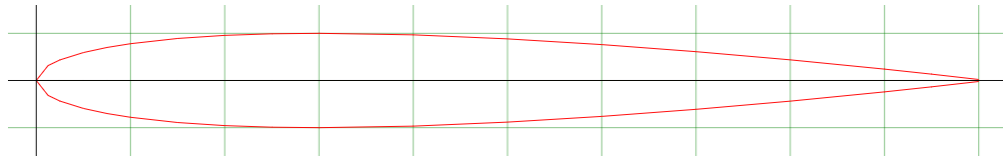
Figure 3.17 Airfoil NACA0012 taken from www.airfoilttols.com.

3.3.4 Tailplane
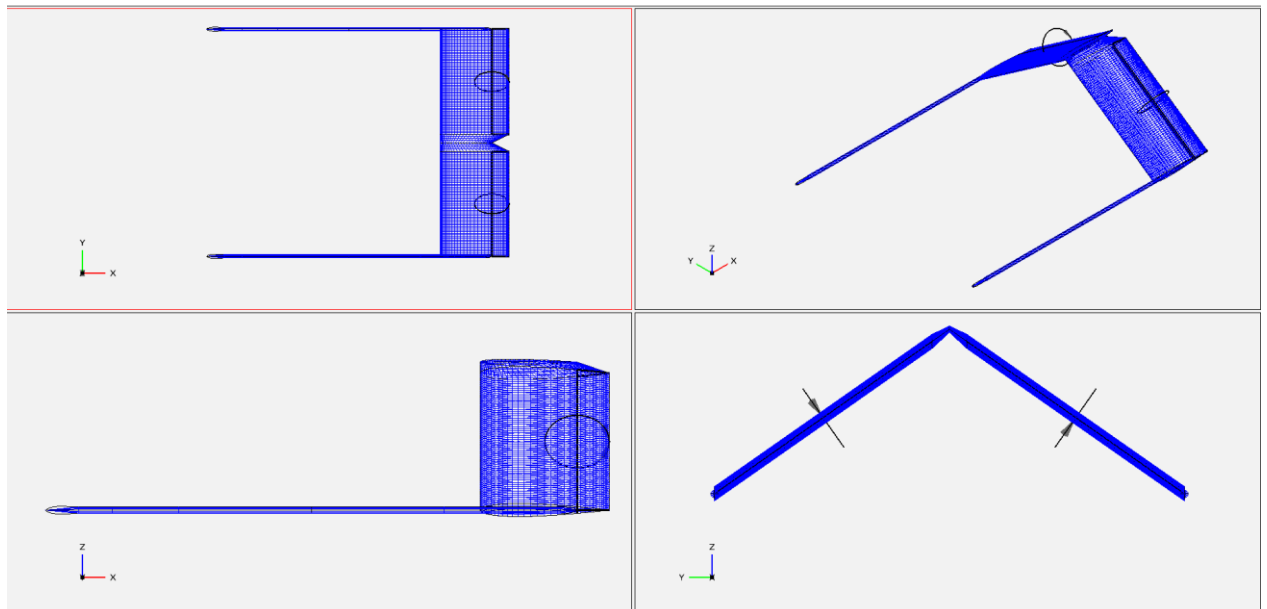
Figure 3.18 Tailplane and booms seen from four points of view.

Note that the booms are symmetric to the XZ plane thus in Figure 3.19 it is presented only one of the two booms parameters. Booms have been modelled as fuselages.

The airfoil selected for the tailplane is the NACA0010 that has been already presented regarding wing's winglets. Tailplane is made up by 2 sections and it present *ruddervators* that will be discussed in the following subsection.
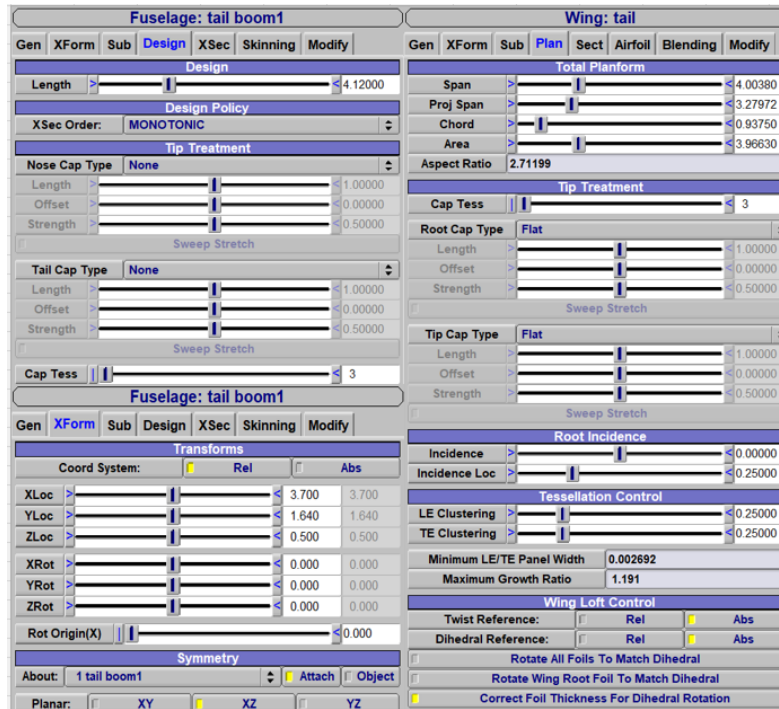
Figure 3.19 Tailplane and booms general parameters.

3.3.5 Control surfaces

OpenVSP lets the user add control surfaces on wings selecting "sub" in the geometry window (Figure 3.20). Grouping and deflection settings must be selected before the analysis in VSPAERO.
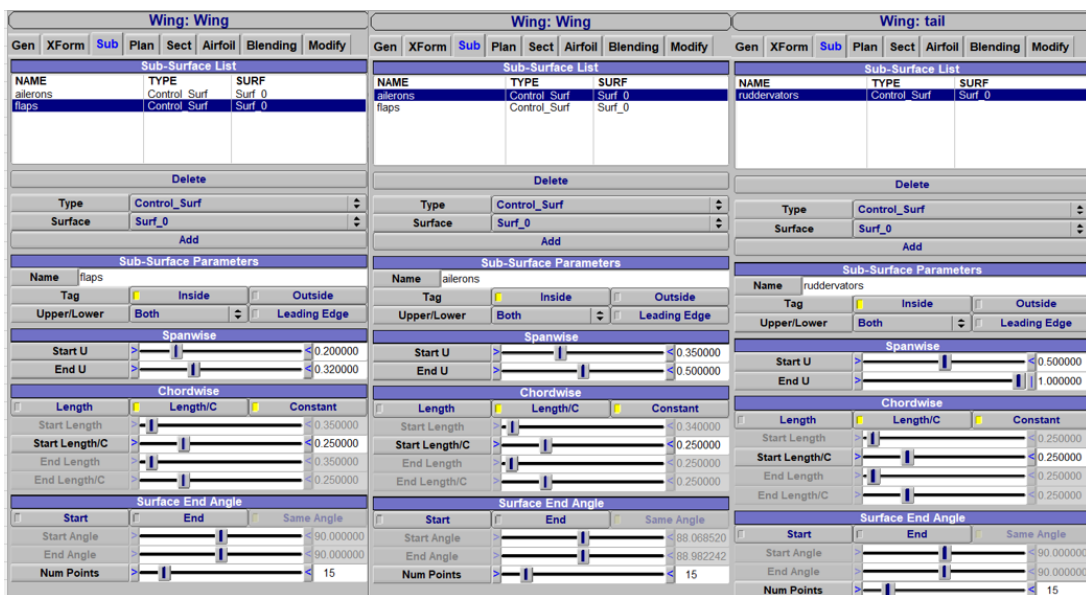
Figure 3.20 Control surfaces geometry settings

VSPAERO considers antisymmetric deflection as default. This means that for flaps it is necessary to invert one of the two deflection gains. As regards *ruddevators*, when the gains are equal they work as rudder, on the other hand, they work as elevator when the gains are opposite.
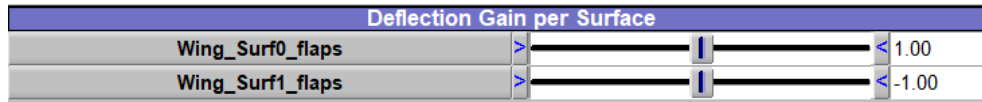
Figure 3.21 Flap gains setting.
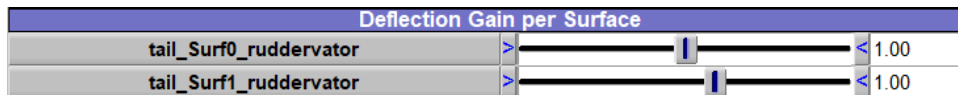
Figure 3.22 ruddervators set as rudder.
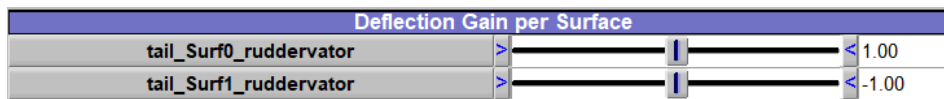
Figure 3.23 ruddervators set as elevator.

3.3.6 Other UAV elements

The geometric model also presents elements not considered in aerodynamic analysis that are propeller and engine exhausts (modelled as open fuselages). In fact, when the work will deal propulsive effects on longitudinal stability in Chapter 6, the propeller will be seen as an actuator disk (Figure 3.26).
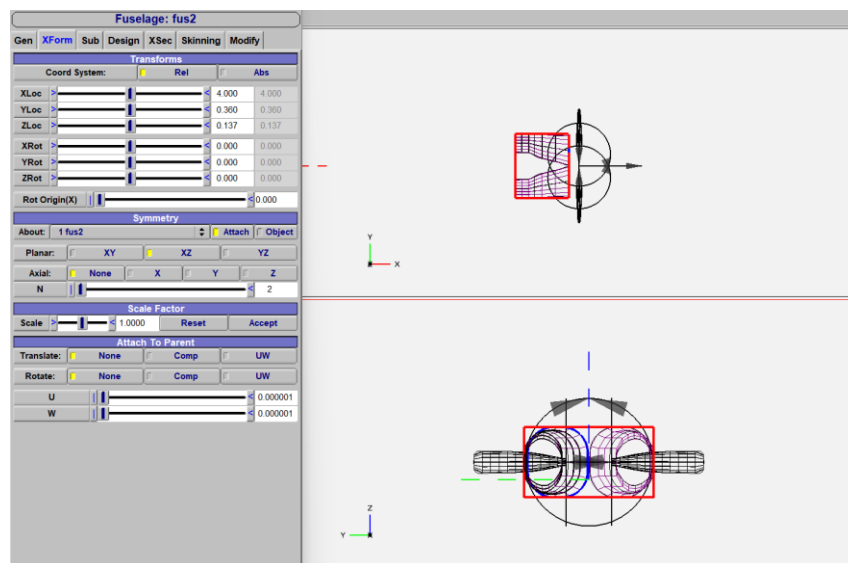
Figure 3.24 PD-1's Engine exhausts seen together to the propeller.
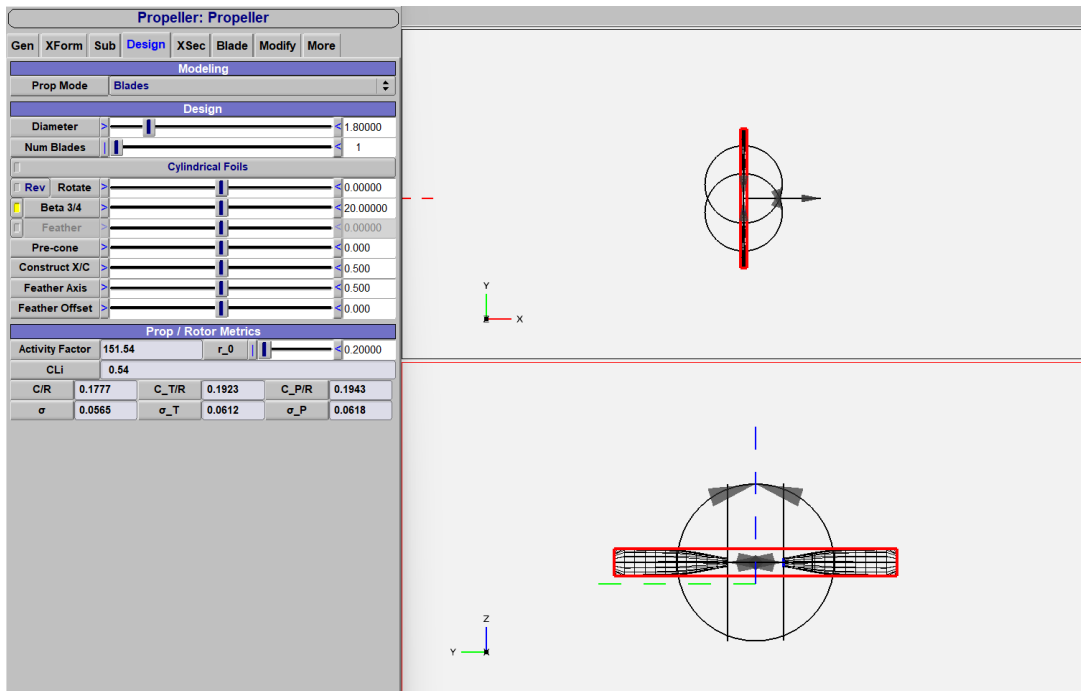
Figure 3.25 PD-1's propeller
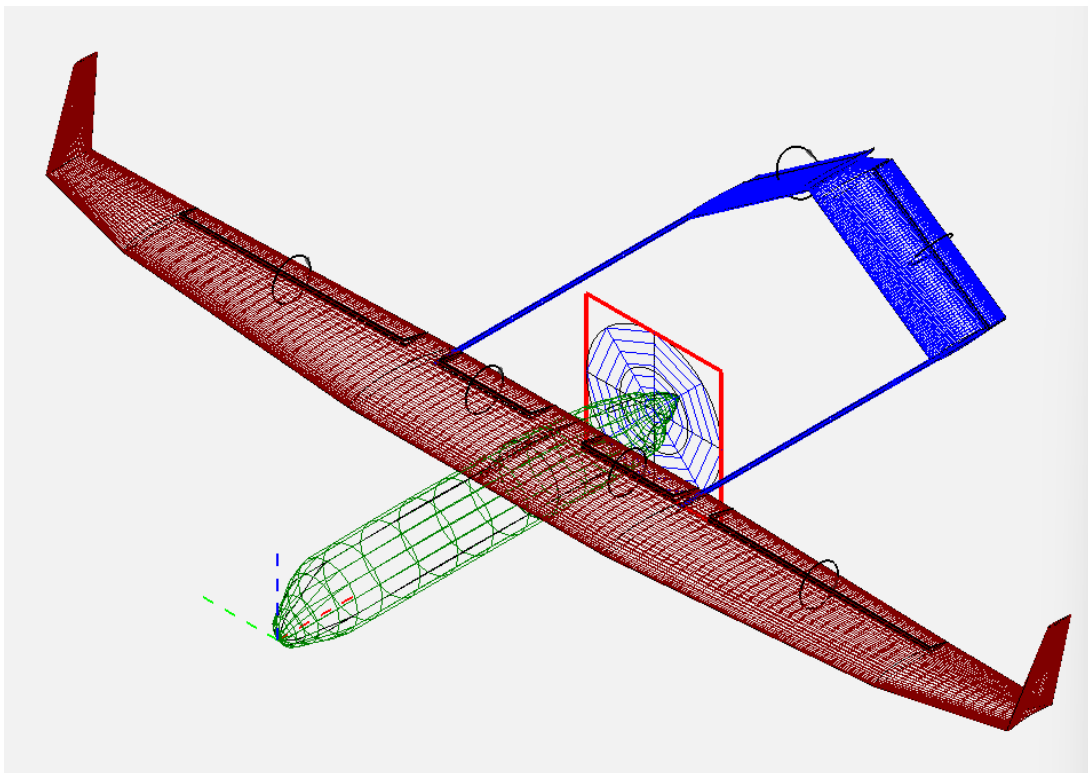
Figure 3.26 PD-1's propeller modelled as an actuator disk

4. Longitudinal Aerodynamics Analysis

Before showing the results of the study let's see how VSPAERO has been set to perform them. The user can find VSPAERO clicking on "analysis" >" aero" in the workspace window (Figure 3.1). VSPAERO lets choose between panel method and VLM as numerical methods. Moment reference position and reference dimension can be selected or evaluated by VSPAERO from the model. Other things that the user can select are flow conditions (Re, M, α, β) and the geometry set to analyze (Figure 4.2). The last aspect to underline is the choice of control surfaces deflections. They can be selected in the "control groups angles" section of VSPAERO browser.

As regards geometry sets to analyze, clicking next to "geometry set" in Figure 4.1, a drop-down browser appears, and the user can choose the previously assigned set. For example, "set 0" in this work has been assigned, in the geometry browser, to the isolated wing.
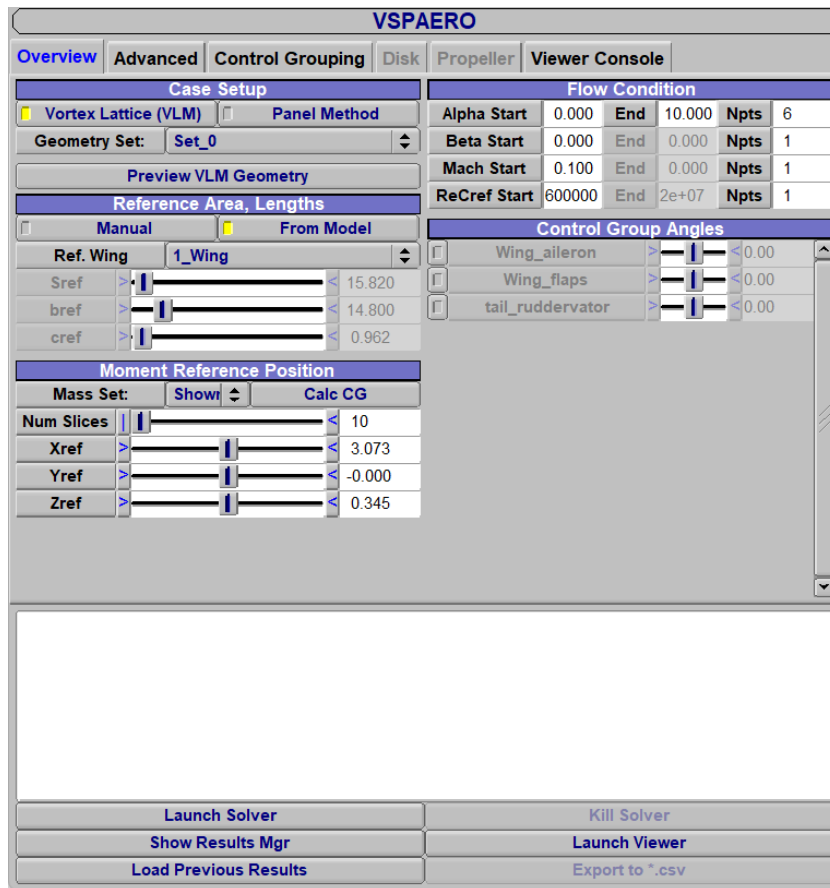
Figure 4.1 VSPAERO settings to perform longitudinal aerodynamics analysis.
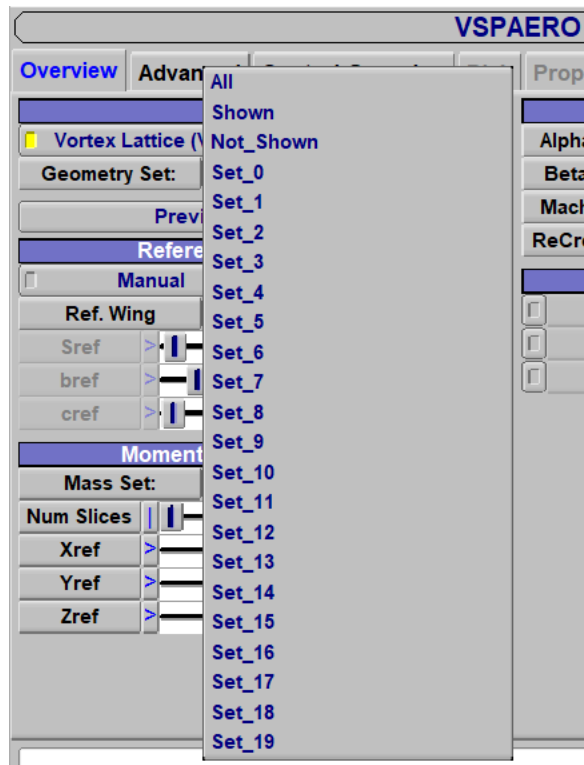
Figure 4.2 geometry set selection.

In this thesis work the longitudinal aerodynamics analysis have been performed using the following condition:

- Reference dimension from the model.
- CG as moment refence position (CG location calculated by VSPAERO)
- Re=600000 and M=0.1 according to PD-1 cruise speed.
- Range of angle of attack α between 0° and 10° with two degrees steps.

VSPAERO collects the data in text files that have been elaborated in excel. The files used in this chapter are:

- LODfiles for wing and tailpane loadings.
- POLARfiles for global aircraft's coefficients.
- STABfiles for control and stability derivatives.

4.1 From the isolated wing to the complete aircraft

In this paragraph are presented comparison between the 3D aerodynamic curves of: isolated wing (W), wing-fuselage combination (WB), wing-fuselage-tailplane combination (WBT) and complete aircraft (including tail booms but still without engine exhaust and propeller). Furthermore, il will be shown the wing loading at different angles of attack α.

Note that control surfaces have been disabled in this analysis.

4.1.1 Lift and Wind Loading

The results obtained from VSPAERO are:

α	C_{LW}	C_{LWB}	C_{LWBT}	C_L
0	0.54	0.54	0.52	0.52
2	0.72	0.72	0.71	0.71
4	0.90	0.89	0.90	0.90
6	1.07	1.07	1.09	1.10
8	1.25	1.24	1.28	1.29
10	1.42	1.41	1.47	1.47

Table 4.1 Lift coefficients

Plotting the data contained in Table 4.1:
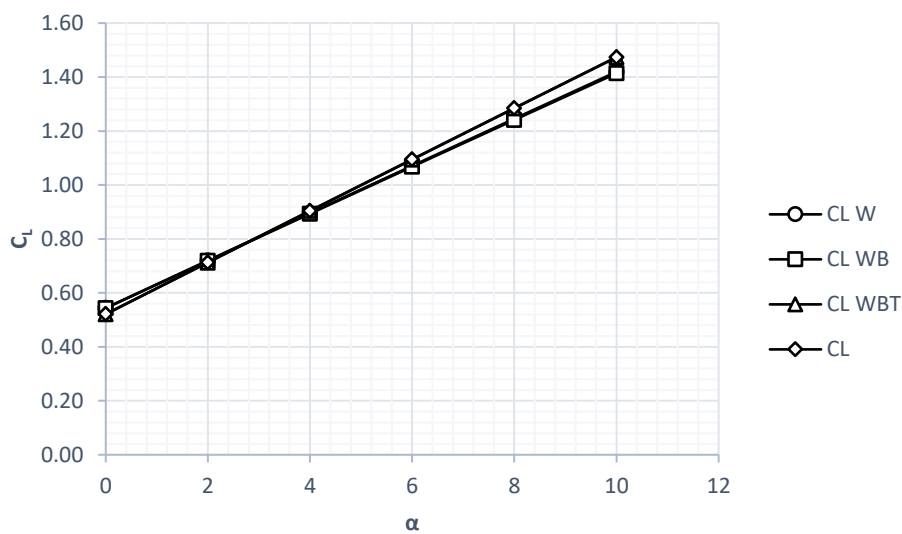
Figure 4.3 Lift coefficients curves

VSPAERO cannot perform stall condition, thus Figure 4.3 represents only the linear section of a real lift coefficient curve.

The global lift coefficient of the isolated wing derives from the wing loading shown in the picture below. Note that the latter is presented only along the right half-wing and it is shown in its dimensionless form as the wingspan.
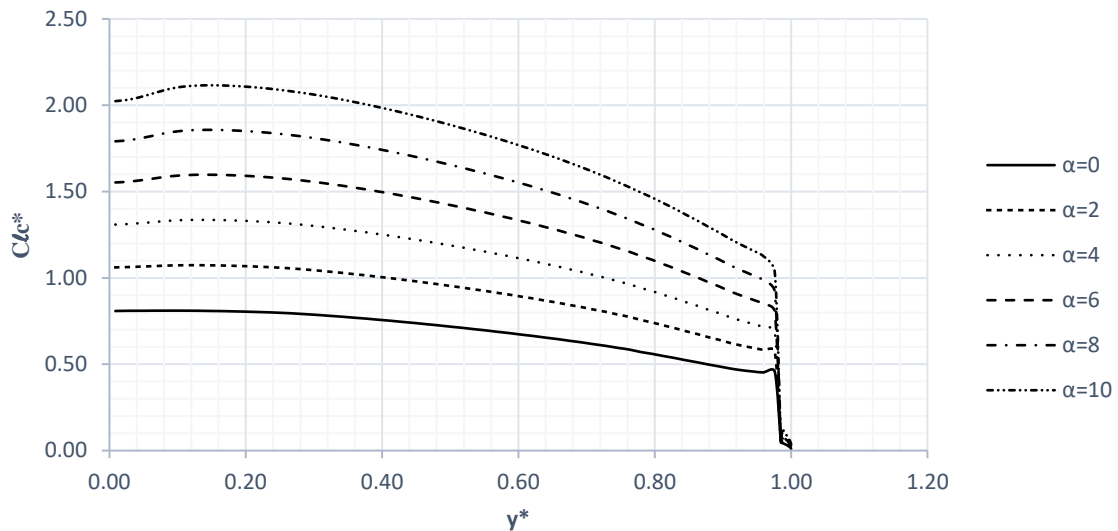
Figure 4.4 Wing loading of the isolated wing

Watching Figure 4.3 and reading Table 4.1 it is possible to evidence that fuselage and tail booms don't alter lift properties of the wing and that the linear behaviour is conserved in all the cases considered. From the last column of Table 4.1, applying the Excel slope function, we can get $C_{L\alpha}$ that is the total aircraft's lift curve slope.

$$C_{L\alpha} = 0.10 \qquad (4.1)$$

Furthermore, opening "lunch viewer" in VSPAERO browser (Figure 4.1) it is possible to see trailing wakes and pressure distribution on the model.
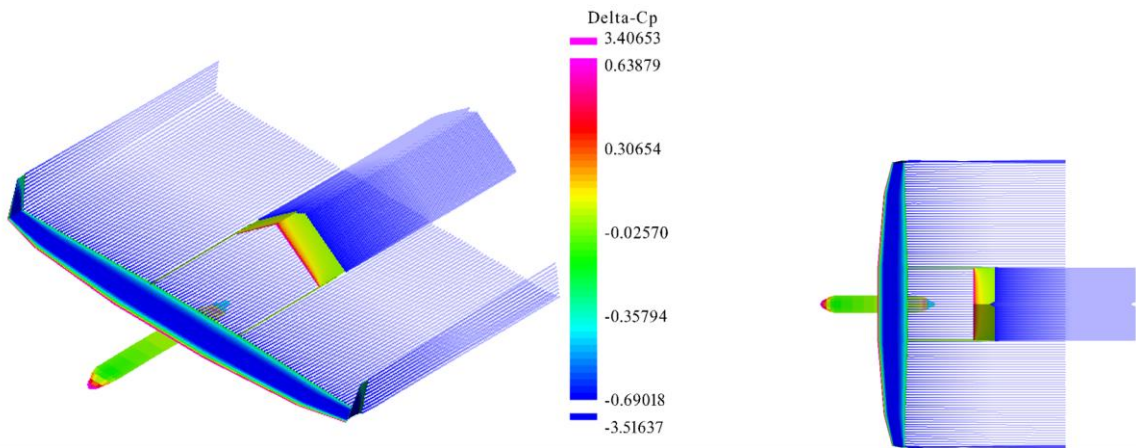
Figure 4.5 pressure distribution and trailing wakes of the complete aircraft

4.1.2 Pitching Moment

α	C_{MW}	C_{MWB}	C_{MWBT}	C_M
0	-0.077	-0.186	-0.0928	-0.0930
2	-0.039	-0.184	-0.1570	-0.1577
4	0.000	-0.184	-0.2242	-0.2251
6	0.038	-0.186	-0.2945	-0.2951
8	0.077	-0.190	-0.3678	-0.3685
10	0.115	-0.196	-0.4439	-0.4442

Table 4.2 Pitching moment coefficients.
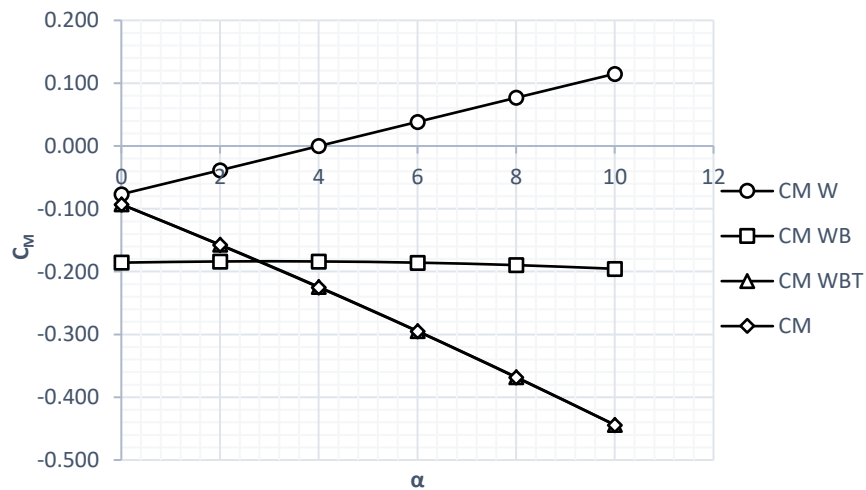
Figure 4.6 C_M vs α curve for each configuration

As regards pitch momentum, looking at Table 4.2 and Figure 4.6 it is notable:

- Isolated wing has an unstable behavior that the fuselage turns into neutral.
- Tail booms affect C_M only at its third/fourth decimal.
- The PD-1 is longitudinally stable having C_M a negative slope through the equilibrium point [1]

Matching table 4.1 with table 4.2 it is possible to obtain the chart below:
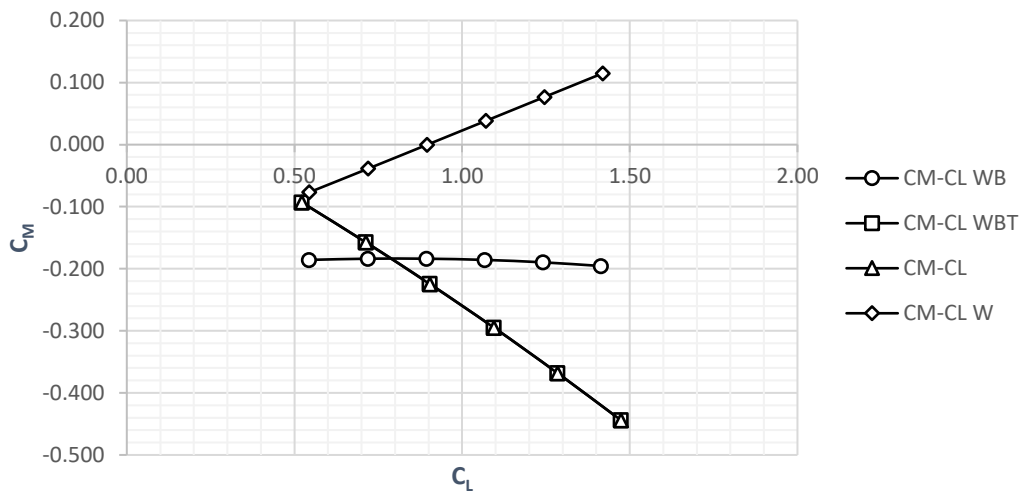
Figure 4.7 C_M vs C_L curve for each configuration

From the last column of Table 4.2, applying the Excel slope function, we can get $C_{M\alpha}$ that is the total aircraft's pitching moment curve slope. As predictable from the table, it is negative.

$$C_{M\alpha} = -0.04 \tag{4.2}$$

Knowing the validity of the Equation 4.3:

$$C_{M\alpha} = C_{L\alpha}(\bar{X}_G - \bar{X}_N) \tag{4.3}$$

And recalling Equation 4.4:

$$SM = (\bar{X}_G - \bar{X}_N) \tag{4.4}$$

where $\bar{X}_G$ and $\bar{X}_N$ are respectively centre of gravity and neutral point dimensionless locations in constructive axes (origin in the nose, x axis towards the fuselage stern, y axis towards the right half-wing, z axis positive upward).

It's possible to create the following table:

item	Value
X_G	3.073
$C_{L\alpha}$	0.10
$C_{M\alpha}$	-0.04
SM	-0.37
X_N	3.43

Table 4.3 Stability derivatives and neutral point

It is easy to see that SM is negative and then the centre of gravity is placed ahead the neutral point. That newly confirms that the PD-1 is statically stable.

4.1.3 Drag and aerodynamic efficiency

α	C_{DW}	C_{DWB}	C_{WBT}	C_D
0	0.021	0.021	0.023	0.023
2	0.028	0.028	0.031	0.031
4	0.037	0.038	0.041	0.041
6	0.048	0.049	0.054	0.054
8	0.061	0.062	0.069	0.069
10	0.076	0.077	0.086	0.086

Table 4.4 Drag coefficients.

It is easy to see how fuselages effects to drag are truly little and this stems from the way VSPAERO compute drag. In fact, only induced drag is calculated by the tool thus only lifting surfaces gives relevant contribution to drag. In figure 4.8 is displayed the drag polar of the different configurations.
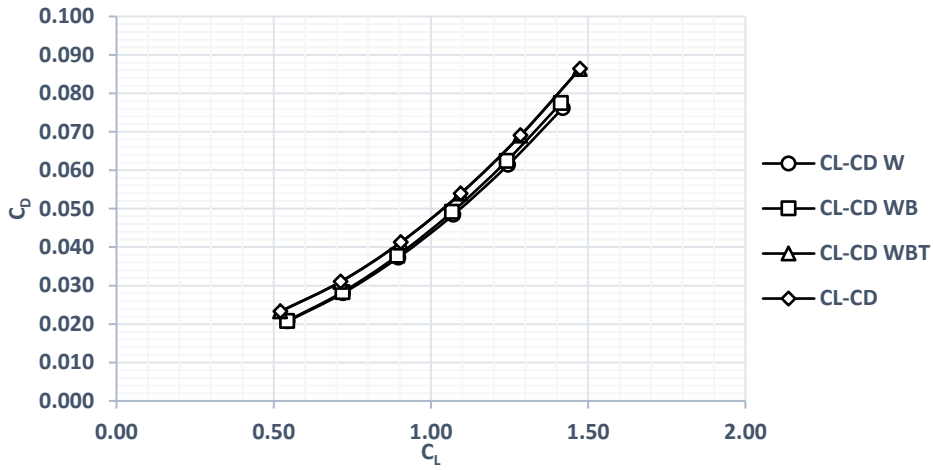
Figure 4.8 PD-1's polar drag

As regards aerodynamic efficiency E (lift-to-drag ratio):

α	E_W	E_{WB}	E_{WBT}	E
0	26.27	26.08	22.37	22.40
2	25.70	25.38	22.98	22.99
4	24.04	23.65	21.91	21.91
6	22.13	21.71	20.29	20.29
8	20.29	19.88	18.61	18.61
10	18.64	18.25	17.06	17.06

Table 4.5 Aerodynamic efficiency
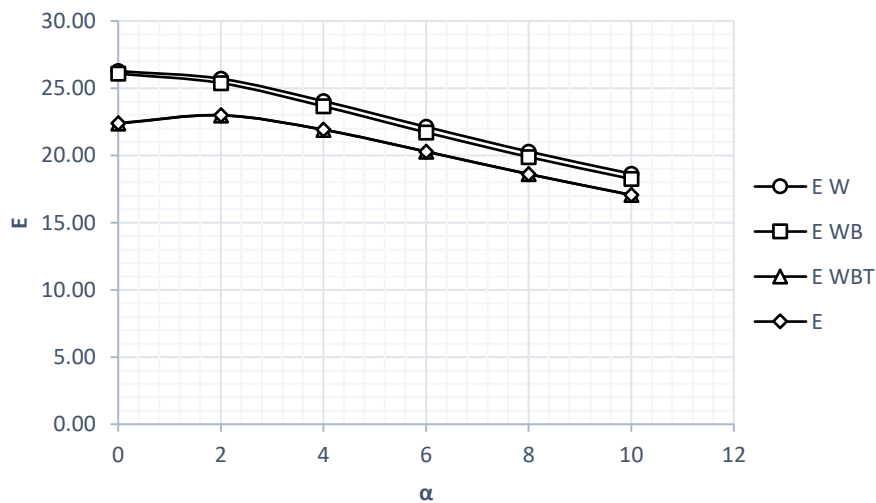
Figure 4.9 Aerodynamic Efficiency

4.2 High-lift devices effects on longitudinal aerodynamics

The aim of this analysis is to display the effects of flaps deflection δ_f over the performance shown in the previous section. The analyses have been conducted with $\delta_f=15°$ and $\delta_f=30°$ and the results compared with the case of no deflection. As shown previously to make this tests δ_f has been selected in the "control group angles" section of VSPAERO and it has been imposed an inverted angles gain for the surfaces to obtain a symmetric deflection.

4.2.1 Lift and Wind Loading

α	$C_{L,\delta f=0°}$	$C_{L,\delta f=15°}$	$C_{L,\delta f=30°}$
0	0.52	0.65	0.74
2	0.71	0.83	0.92
4	0.90	1.03	1.11
6	1.10	1.22	1.31
8	1.29	1.41	1.50
10	1.47	1.60	1.69

Table 4.6 Lift coefficients vs δ_f
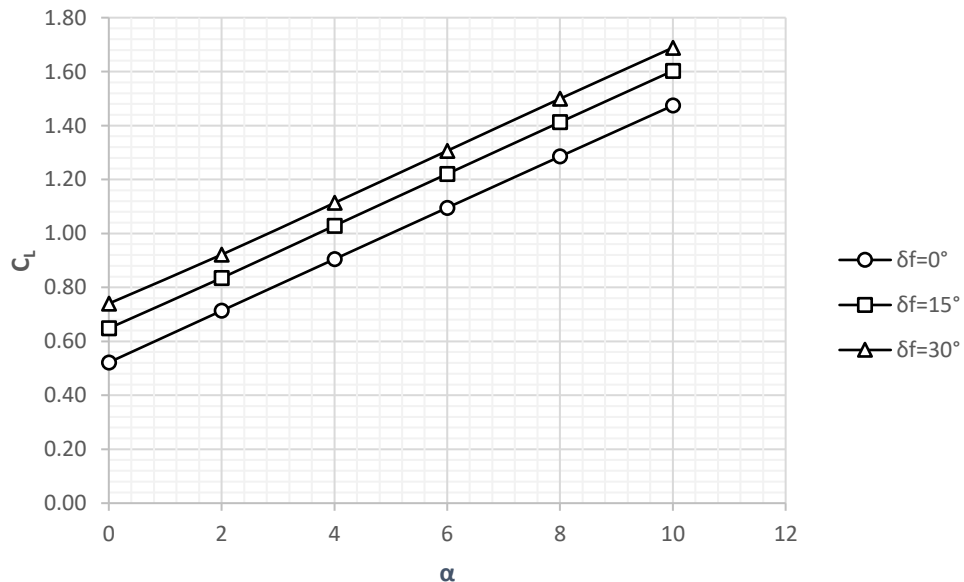
Figure 4.10 Lift coefficients

Note that δ_f does not affect $C_{L\alpha}$, in fact, the three lines are parallel and translated upward. Flaps effects over lift are reassumed in the table below:

item	value
$\Delta C_{L0\ (\delta f\ 0°\rightarrow15°)}$	0.13
$\Delta C_{L0\ (\delta f\ 15°\rightarrow30°)}$	0.22
$C_{L\delta f}$	0.01deg^{-1}
$\alpha_{0L\ (\delta f\ =0°)}$	-5.48°
$\alpha_{0L\ (\delta f\ =15°)}$	-6.78°
$\alpha_{0L\ (\delta f\ =30°)}$	-7.77°

Table 4.7 Effects of flaps deflection on lift

The term $C_{L\delta f}$ has been estimated using the following equation:

$$C_{L\delta f} = \frac{C_{L,\delta f=15°} - C_{L,\delta e=0°}}{15} \tag{4.5}$$

By now all the control derivatives will be evaluated exploiting this method.

The next chart will show wing loading modifications caused by flaps deflections at α=0.
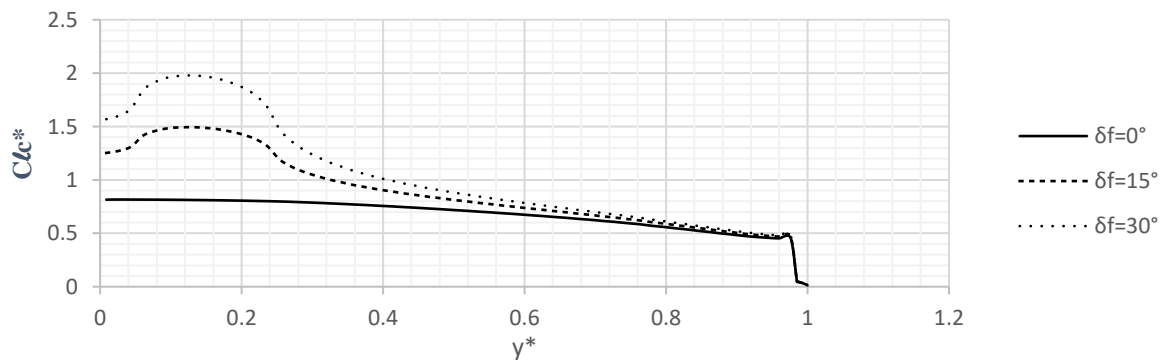
Figure 4.11 wing loading at different flap deflections (α=0)

Launching the viewer for δ_f=15 °and δ_f=30°, the differences from the non-deflected flaps case shown in Figure 4.5 are:

- Different behaviour of the trailing wakes around flaps section.
- Lower ΔC_P on the wing with flaps activated. This means more wing loading.
- Higher ΔC_P on the tailplane in flaps activated cases. This means that the tailplane increases its downforce with δ_f like the elevator were deflected (Figure 4.13). We will go into detail about this point dealing with pitching moment in next sub-section.
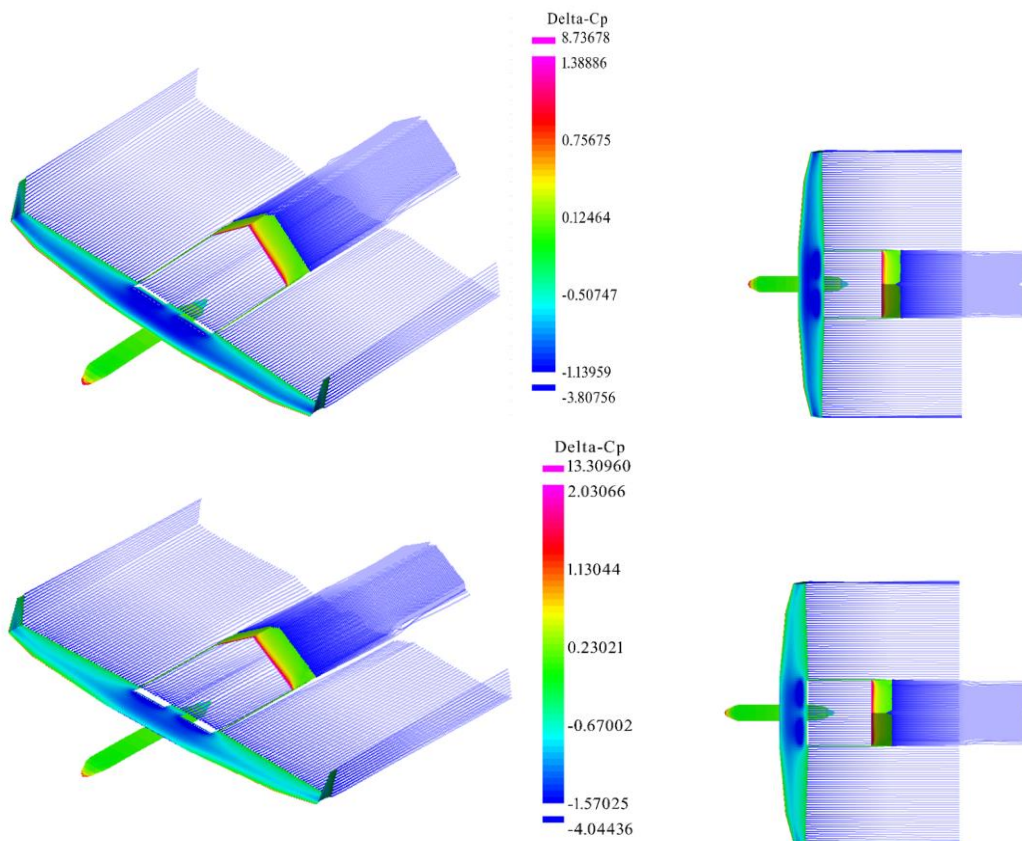
Figure 4.12 Pressure distributions and trailing wakes for δ_f=15$^\bullet$ and δ_f=30$^\bullet$
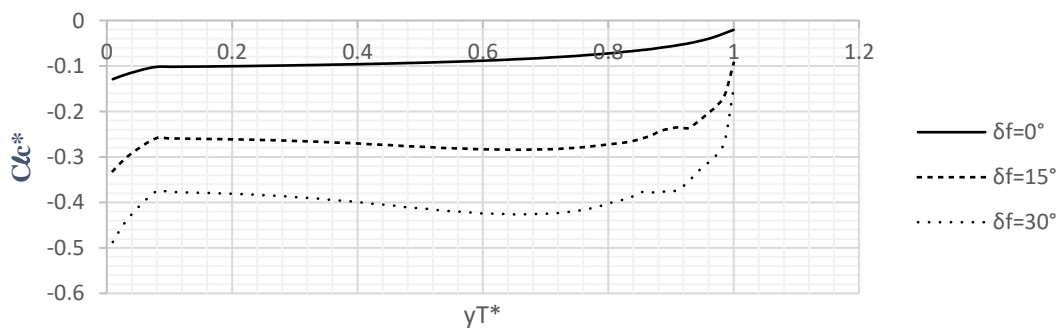
Figure 4.13 Tailpane loading vs δ_f

4.2.2 Pitching Moment

α	$C_{M,\delta f=0°}$	$C_{M,\delta f=15°}$	$C_{M,\delta f=30°}$
0	-0.093	0.063	0.176
2	-0.158	0.019	0.145
4	-0.225	-0.077	0.044
6	-0.295	-0.166	-0.067
8	-0.368	-0.257	-0.180
10	-0.444	-0.350	-0.281

Table 4.8 Pitching moment vs δ_f
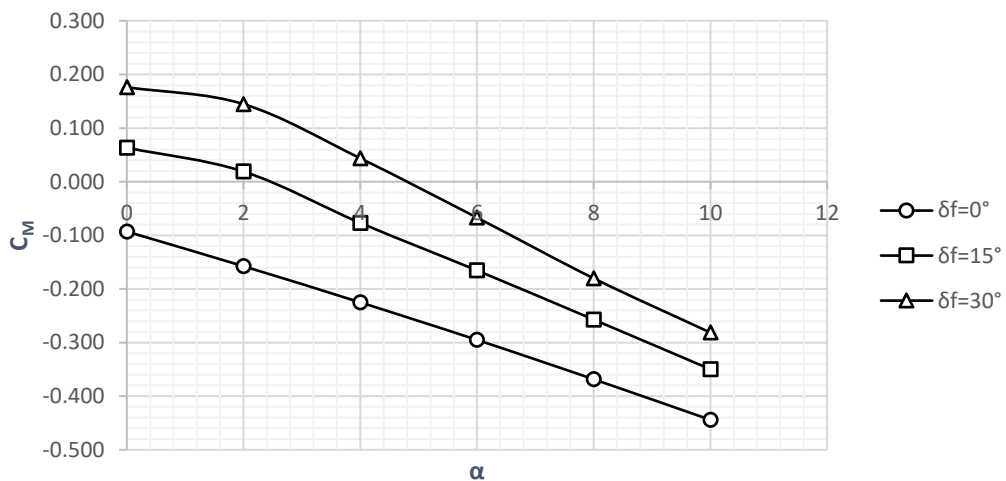
Figure 4.14 C_M vs α curve for each δ_f

The positive $C_{M\delta f}$ is an unusual behavior that came out from the tailplane response to increasing δ_f. The tailplane, producing more and more downforce, brings the aircraft to pitch-up since this force is applied behind the CG. That means that C_{M0} moves upward on the chart with increasing δ_f.

This attitude is probably related to the unusual shape of the tail and to the relative tailplane-wing position, but this work will not focus more on that. Combining Table 4.6 and Table 4.8 it is possible to obtain the C_M vs C_L chart. This displays the same uncommon attitude of C_M vs α chart: the curves move upward with δ_f.
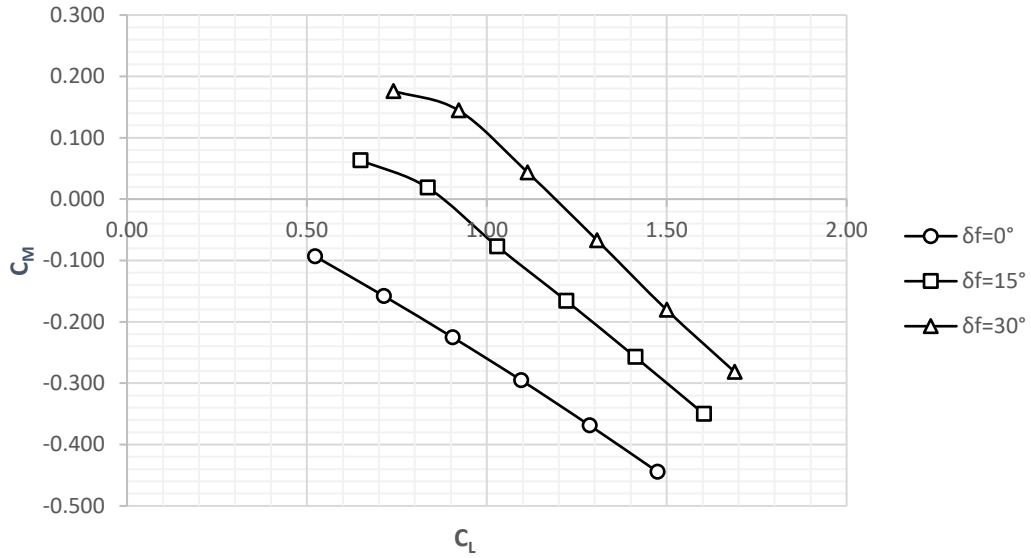
Figure 4.15 C_M vs C_L curve for each δ_f

4.2.3 Drag and aerodynamic efficiency

α	$C_{D,\delta f=0°}$	$C_{D,\delta f=15°}$	$C_{D,\delta f=30°}$
0	0.023	0.031	0.040
2	0.031	0.040	0.050
4	0.041	0.052	0.062
6	0.054	0.067	0.079
8	0.069	0.084	0.098
10	0.086	0.104	0.118

Table 4.9 Drag coefficient vs δ_f

As expected, since lift and δ_f are proportional, induced drag seen by VSPAERO increases too.

Figure 4.16 displays drag polars at different δ_f:
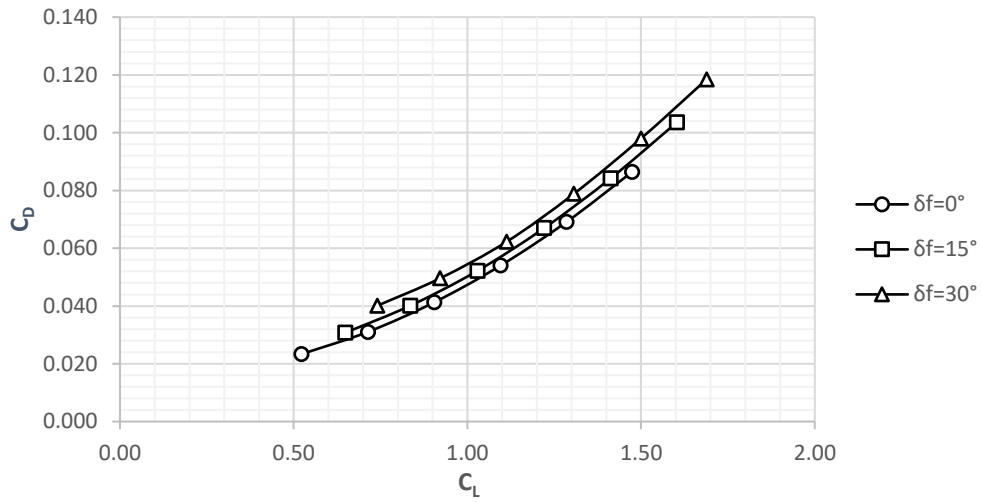
Figure 4.16 polar drag for each δ_f

As regards flaps effect on aerodynamic efficiency:

α	$E,_{\delta f=0°}$	$E,_{\delta f=15°}$	$E,_{\delta f=30°}$
0	22.40	21.09	18.47
2	22.99	20.83	18.58
4	21.91	19.72	17.88
6	20.29	18.23	16.57
8	18.61	16.78	15.31
10	17.06	15.48	14.26

Table 4.10 Aerodynamic efficency vs δ_f
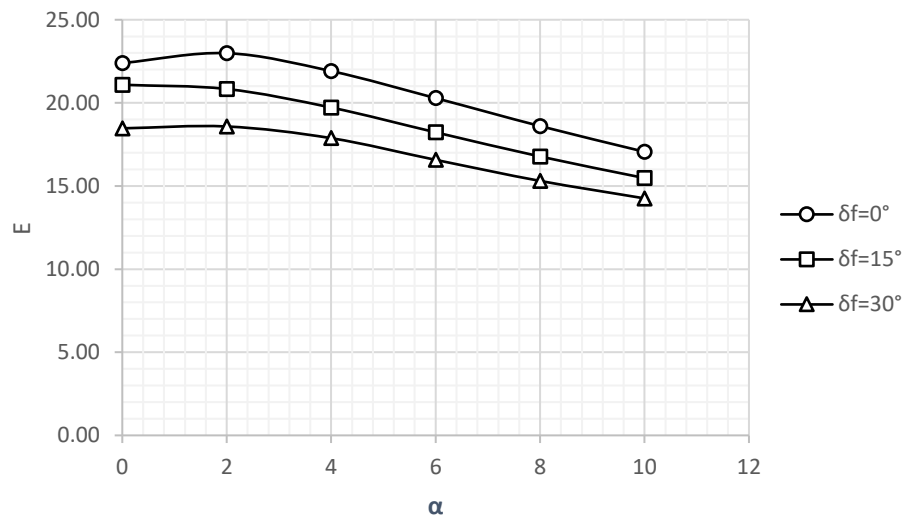
Figure 4.17 Aerodynamic efficency for each δ_f

4.3 Ruddervators effects on longitudinal aerodynamics

The aim of this analysis is displaying the effects of the *ruddervators* deflection over the longitudinal aerodynamic performance. The analyses have been conducted both with symmetric deflection and with antisymmetric deflection. The section will analyze how elevator control pitching moment (antisymmetric deflection of *ruddervators* set on VSPAERO) and it will value unwanted effects of rudder on longitudinal stability too (antisymmetric deflection of *ruddervators* set on VSPAERO). The tests have been made with the following deflections set:

- δ_e=0°, -10°, -20°, -30°.
- δ_r=0°,10°,20°,30°.

4.3.1 Lift and Tailplane Loading

α	$C_{L,\delta e=0°}$	$C_{L,\delta e=-10°}$	$C_{L,\delta e=-20°}$	$C_{L,\delta e=-30°}$
0	0.52	0.44	0.37	0.32
2	0.71	0.63	0.56	0.51
4	0.90	0.82	0.75	0.70
6	1.10	1.02	0.94	0.89
8	1.29	1.21	1.13	1.08
10	1.47	1.40	1.32	1.27

Table 4.11 Lift coefficients vs δ_e
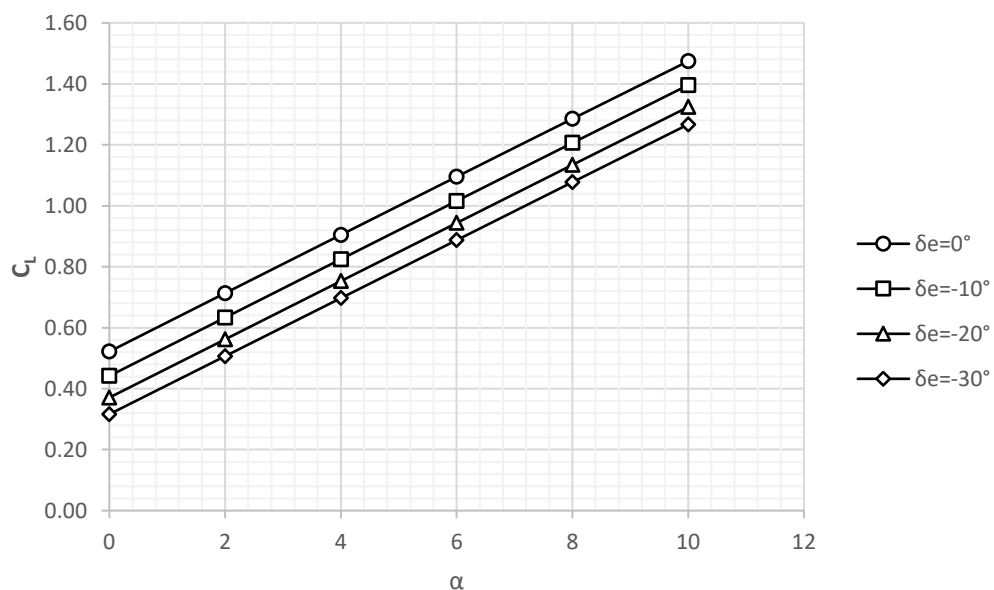
Figure 4.18 Lift coefficients

Negative and symmetric deflections of the *ruddervators* imply more downforce on the tailplane and then low lift coefficients of the global aircraft (Figure 4.18). In Figure 4.19 it is shown the tailplane loading at various δ_e. Note how both flaps and elevator, although in a different way, move downward the tailplane's wing loading increasing the tailplane's downforce.
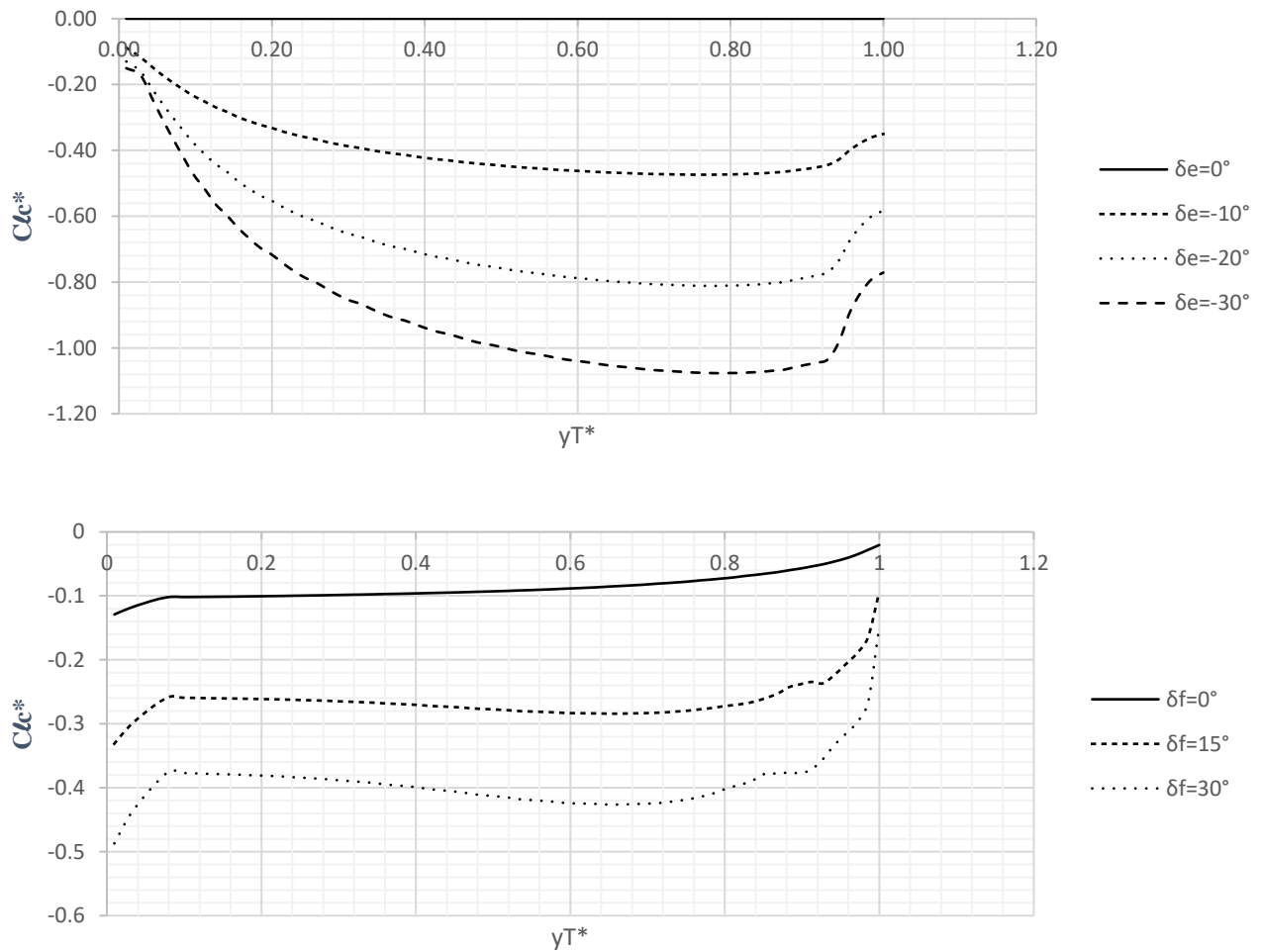
Figure 4.19 tailplane's wing loading: flaps vs elevator

How the wing loading changes is clearly viewable in the following picture realized launching the viewer. In Figure 4.20 pressure distributions and trailing wakes are compared for δe=0° and δe=-20°.
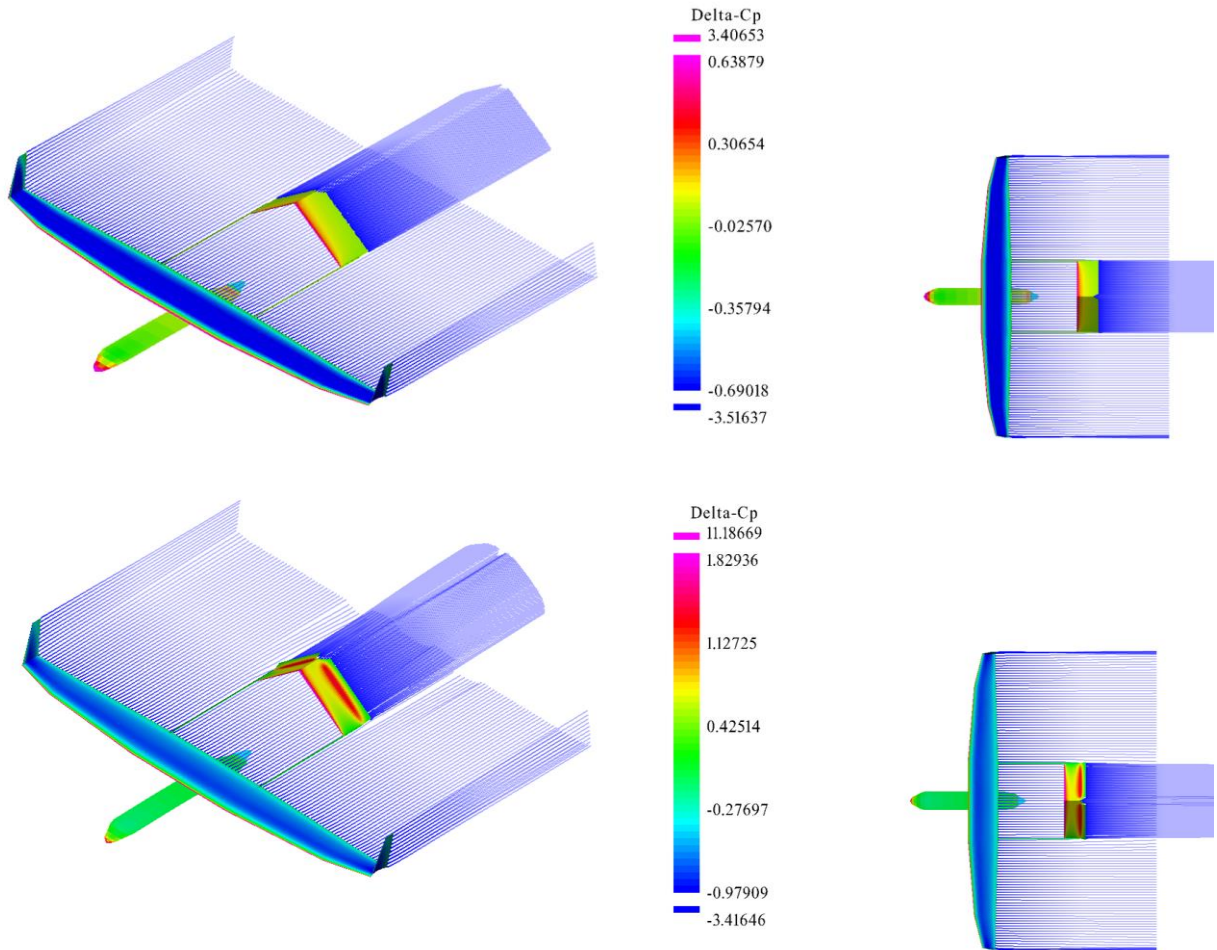
Figure 4.20 pressure distribution and trailing wakes for $\delta_e=0^\bullet$ and $\delta_e=-20^\bullet$

Other than the increasing downforce on the tailplane with δ_e it is easy to see even a little lower ΔC_P on the wing. This means that even the wing is generating less lift.

Using the data contained in Table 4.11we can get $C_{L\delta e}$ which is the control derivatives of lift using elevators.

$$C_{L\delta e} = 0.0080 \text{ deg}^{-1} \tag{4.6}$$

As expected, it is positive and this means that with negative deflections (as we dealt previously) the lift decreases.

Before dealing with the pitching moment, let's see if antisymmetric deflections of the *ruddervators* alter lift generation of the PD-1. This doubt arises from the shape of the tailplane and consequently from the unusual control surfaces PD-1 uses. It is clear looking Table 4.12 and Table 4.13 that *ruddervators* used as a rudder do not affect aircraft capability of producing lift.

α	$C_{L,\delta r=0°}$	$C_{L,\delta r=10°}$	$C_{L,\delta r=20°}$	$C_{L,\delta r=30°}$
0	0.52	0.52	0.52	0.52
2	0.71	0.71	0.71	0.71
4	0.90	0.90	0.90	0.90
6	1.10	1.09	1.09	1.09
8	1.29	1.28	1.28	1.28
10	1.47	1.47	1.47	1.46

Table 4.12 rudder effects on C_L at different angles of attack

β	$C_{L,\delta r=0°}$	$C_{L,\delta r=10°}$	$C_{L,\delta r=20°}$	$C_{L,\delta r=30°}$
0	0.52	0.52	0.52	0.52
2	0.52	0.52	0.52	0.52
4	0.52	0.52	0.52	0.52
6	0.52	0.52	0.52	0.52
8	0.51	0.51	0.52	0.52
10	0.51	0.51	0.51	0.51

Table 4.13 rudder effects on C_L at different sideslip angles

4.3.2 Pitching Moment

α	$C_{M,\delta e=0°}$	$C_{M,\delta e=-10°}$	$C_{M,\delta e=-20°}$	$C_{M,\delta e=-30°}$
0	-0.093	0.256	0.569	0.810
2	-0.158	0.192	0.507	0.751
4	-0.225	0.125	0.440	0.688
6	-0.295	0.054	0.371	0.620
8	-0.368	-0.020	0.297	0.547
10	-0.444	-0.098	0.219	0.470

Table 4.14 Pitching moment vs δ_e
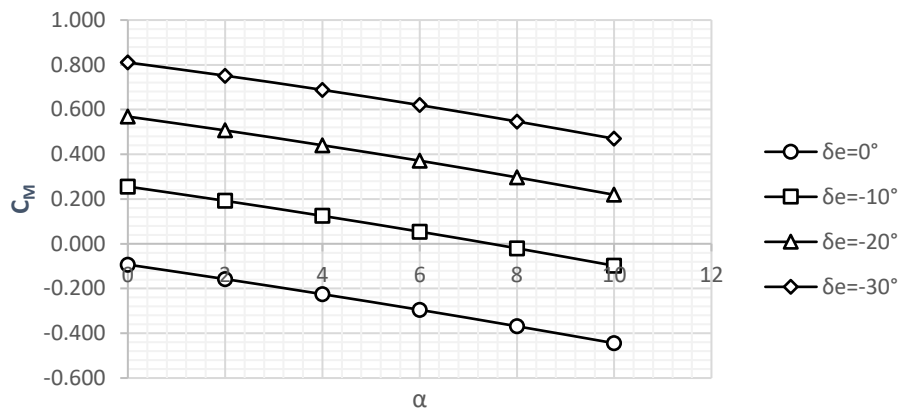
Figure 4.21 C_M vs α curve for each δ_e

As predictable, C_{M0} moves upward with negatives δ_e since these deflections increase tailplane's downforce. This behavior is the same already described for flaps deflections.

Combining Table 4.11 and Table 4.14 it is possible to obtain the C_M vs C_L chart:
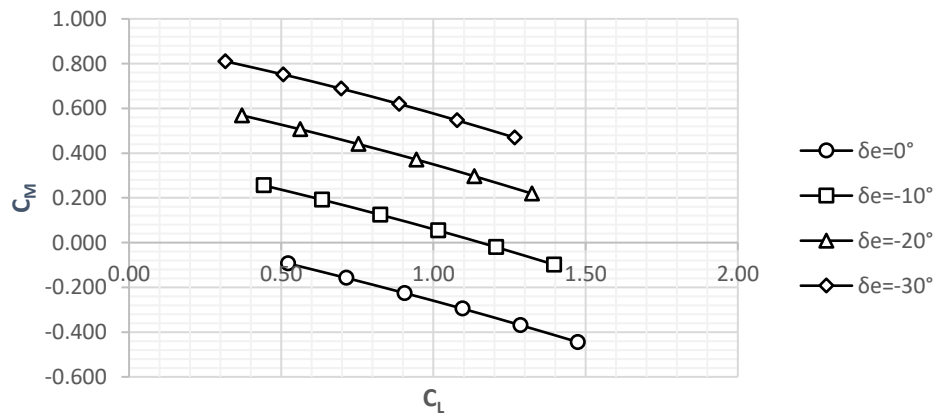
Figure 4.22 C_M vs C_L curve for each δ_f

48

The estimated value for the control derivate $C_{M\delta e}$ is:

$$C_{M\delta e} = 0.0349 \text{ deg}^{-1} \tag{4.7}$$

The negative value means that negative deflections of elevator increase C_M as expected.

As done with lift, let's see if antisymmetric deflections of the *ruddervators* alter pitching moment of the PD-1. It's clear watching Table 4.15 and Table 4.16 that *ruddervators* used as a rudder do not affect pitching moment significantly.

α	$C_{M,\delta r=0°}$	$C_{M,\delta r=10°}$	$C_{M,\delta r=20°}$	$C_{M,\delta r=30°}$
0	-0.093	-0.091	-0.088	-0.083
2	-0.158	-0.155	-0.149	-0.142
4	-0.225	-0.222	-0.213	-0.204
6	-0.295	-0.290	-0.280	-0.268
8	-0.368	-0.362	-0.350	-0.336
10	-0.444	-0.437	-0.423	-0.407

Table 4.15 rudder effects on C_M at different angles of attack

β	$C_{M,\delta r=0°}$	$C_{M,\delta r=10°}$	$C_{M,\delta r=20°}$	$C_{M,\delta r=30°}$
0	-0.093	-0.091	-0.088	-0.083
2	-0.091	-0.091	-0.090	-0.086
4	-0.088	-0.090	-0.089	-0.087
6	-0.084	-0.087	-0.088	-0.087
8	-0.079	-0.084	-0.086	-0.086
10	-0.077	-0.083	-0.087	-0.087

Table 4.16 rudder effects on C_M at different sideslip angles

4.3.3 Drag and aerodynamic efficiency

α	$C_{D,\delta e=0°}$	$C_{D,\delta e=-10°}$	$C_{D,\delta e=-20°}$	$C_{D,\delta e=-30°}$
0	0.023	0.025	0.032	0.041
2	0.031	0.031	0.037	0.044
4	0.041	0.040	0.043	0.050
6	0.054	0.051	0.053	0.058
8	0.069	0.064	0.065	0.068
10	0.086	0.080	0.079	0.081

Table 4.17 Drag coefficient vs δ_e
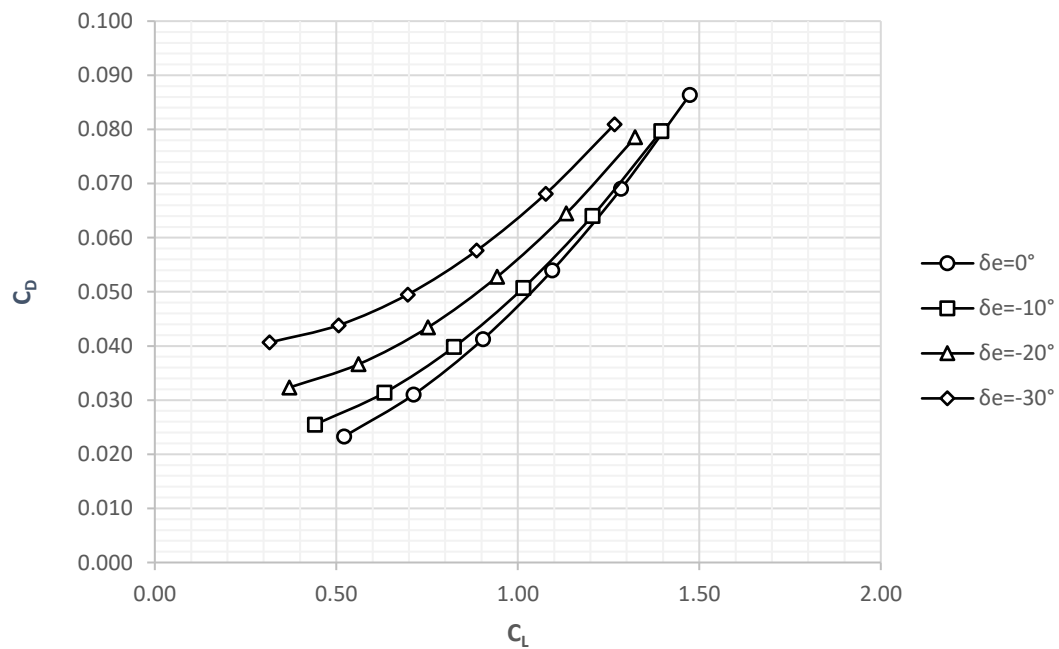
Figure 4.23 Drag polar for each δ_e

By comparing Figure 4.23 and Figure 4.16, we notice that C_D is incremented by the flaps more than by the elevator. Furthermore, C_D is almost constant with δ_e. The last phenomenon stems from the balancing between less global lift and increment of downforce for each consecutive deflection case.

Now it's possible analyse aerodynamic efficiency:

α	$E_{,\delta e=0°}$	$E_{,\delta e=-10°}$	$E_{,\delta e=-20°}$	$E_{,\delta e=-30°}$
0	22.40	17.33	11.47	7.78
2	22.99	20.17	15.33	11.55
4	21.91	20.70	17.33	14.08
6	20.29	20.01	17.87	15.39
8	18.61	18.83	17.58	15.81
10	17.06	17.51	16.85	15.65

Table 4.18 Aerodynamic efficency vs δ_e
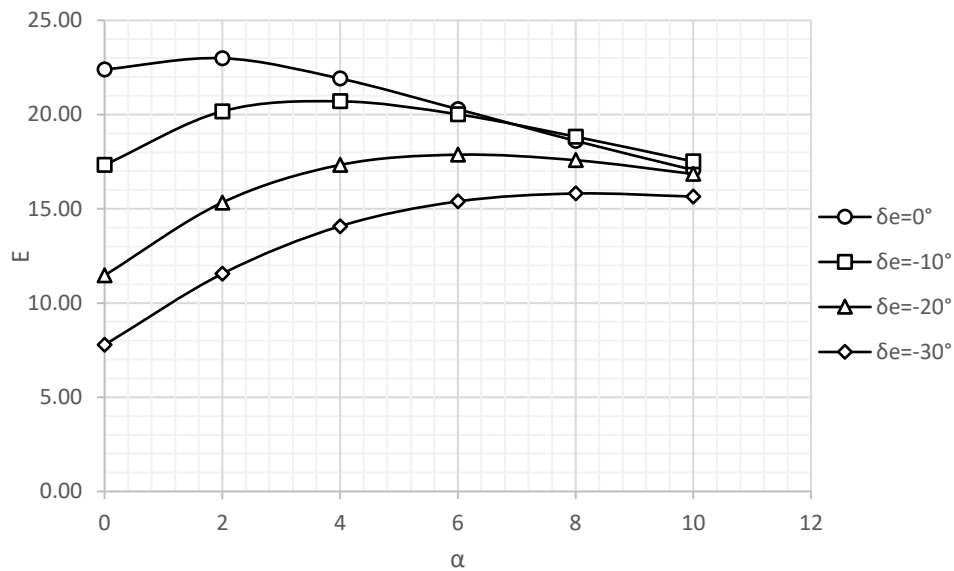
Figure 4.24 Aerodynamic efficency for each δ_e

The huge decrement of E with δ_e came from the attitudes that drag and lift have varying elevator deflections. In fact, drag is almost constant with δ_e while lift decreases with the same parameters. Obviously, this decrement is more important at small value of α because, while at high trims the lift coefficient's differences with δ_e are less significant.

4.4 Longitudinal stability and control derivatives

To obtain the STABfile that contain stability and control derivatives we must run VSPAERO in "steady stability" mode, the latter can be selected in the advanced menu as shown in Figure 4.25. Note that to run VSPAERO in steady mode one must disable the XZ symmetry. What we want to do is comparing VSPAERO results with the ones already estimated in the previous sections.
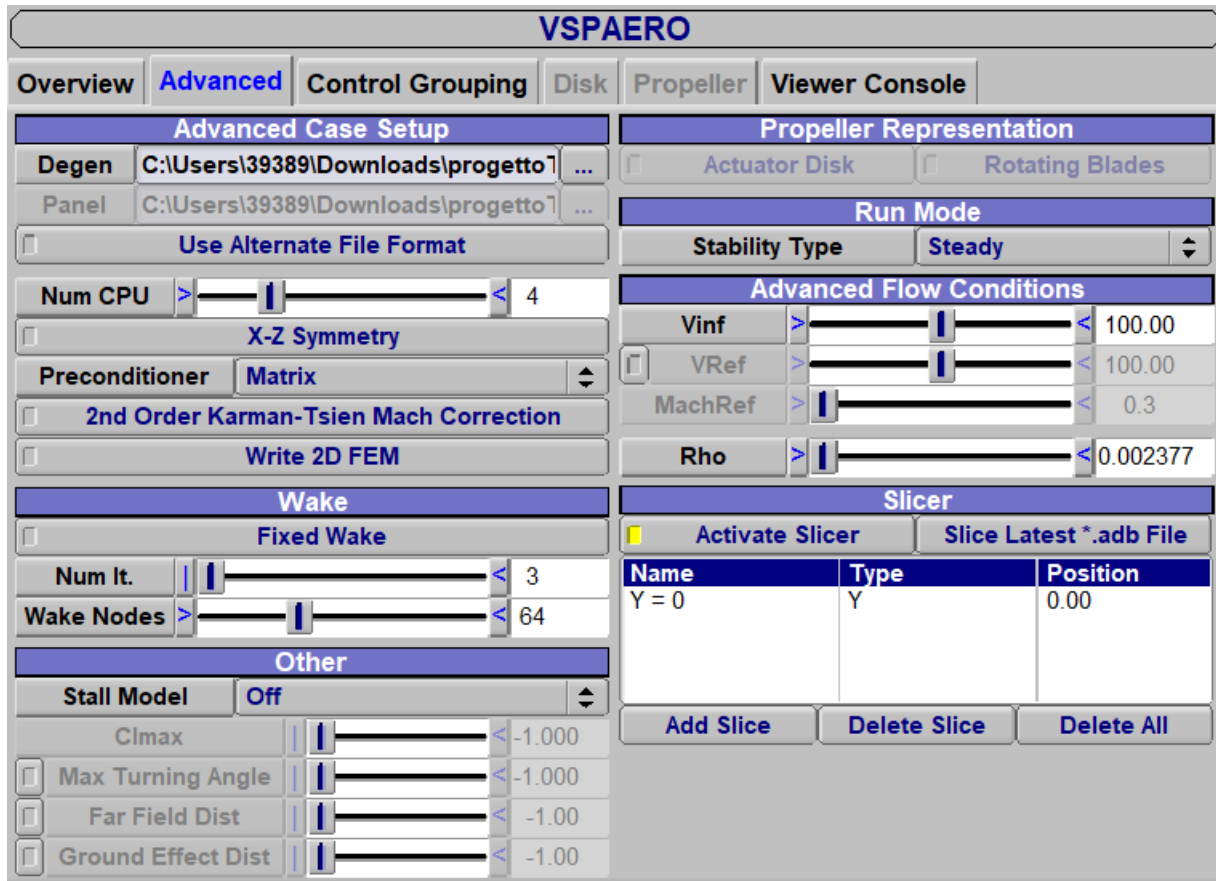
Figure 4.25 advanced menu of VSPAERO

The results obtained are summarized in Table 4.19 (note that the STABfile contains more data but now we are interested only about these).

/	∂C_L	∂C_M
$\partial\alpha$	**0.095**	**-0.031**
∂q	0.214	-0.477
$\partial\delta_e$	**0.008**	**-0.035**
$\partial\delta_f$	**0.009**	0.011

Table 4.19 stability and control derivatives

The values in bold have been already estimated and they are expressed in Equation 4.1, 4.2, 4.6 and 4.7. Comparing them it is possible to display the differences in the table below:

ITEM	STABfile	ESTIMATES	difference %
$C_{L\alpha}$	0.095	0.095	0.0
$C_{M\alpha}$	-0.032	-0.035	10
$C_{L\delta f}$	0.009	0.009	4
$C_{L\delta e}$	0.008	0.008	1
$C_{M\delta e}$	-0.035	-0.035	2

Table 4.20 comparisons of longitudinal derivatives

The stability module of VSPAERO apply a 1 deg variation around the selected α, β and M values and derives the stability derivatives. Therefore, it is a quick approach to evaluate the stability characteristics of an aircraft, but it is considered less accurate of linear regression applied to a larger set of data.

5. Lateral and Directional Aerodynamics Analysis

The conditions used to perform lateral and directional aerodynamic analysis are the same already used for longitudinal analysis. The only differences are that, in this case, we must fix an angle of attack α and let the sideslip angle β vary and we must disable the XZ symmetry in the advanced browser (Figure 4.25). The file used to realise the following tables and charts are the same used in longitudinal analysis, but the data analyzed are different. In fact, the coefficients examined will be:

- Rolling moment coefficient C_R.
- Yawing moment coefficient C_N.
- Sideforce coefficient C_Y.

Furthermore, this chapter deals about the control and stability derivatives of the lateral and directional motion.

5.1 Aircraft behavior without control surfaces deflected

Without using control surfaces, lateral and directional moments and sideforce act as described in the following chart. Obviously, as a result of aircraft's symmetry, each coefficient is very little for $\beta=0$. These values are considered numerical errors due to the discretization of the model in a finite number of lattices.

β	C_R	C_N	C_Y
0	4.1×10^{-5}	3.9×10^{-6}	-1.9×10^{-5}
2	2.1×10^{-3}	-1.3×10^{-3}	-1.4×10^{-2}
4	4.0×10^{-3}	-2.4×10^{-3}	-2.7×10^{-2}
6	6.0×10^{-3}	-3.5×10^{-3}	-4.0×10^{-2}
8	7.9×10^{-3}	-4.6×10^{-3}	-5.2×10^{-2}
10	9.9×10^{-3}	-5.9×10^{-2}	-6.5×10^{-2}

Table 5.1 Natural response of the aircraft with β variations

The charts below will show the coefficients trend with β. Note that VSPAERO compute momentum coefficients in a constructive reference frame so axes X and Z are inverted w.r.t BRF. This means that although C_R and C_N have trends that suggest instability they are not because they are expressed in another reference system.
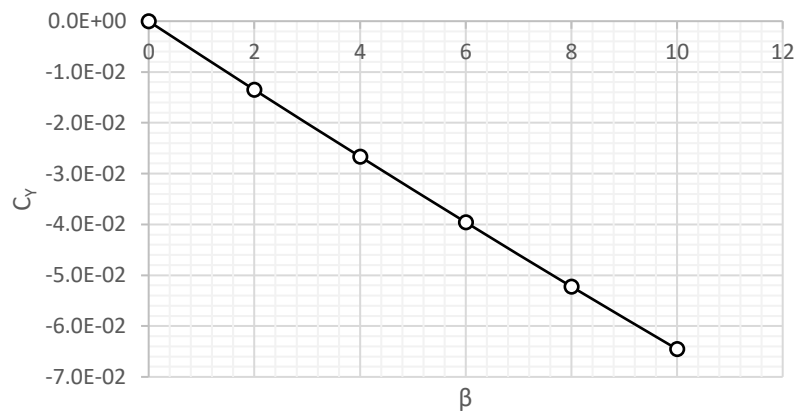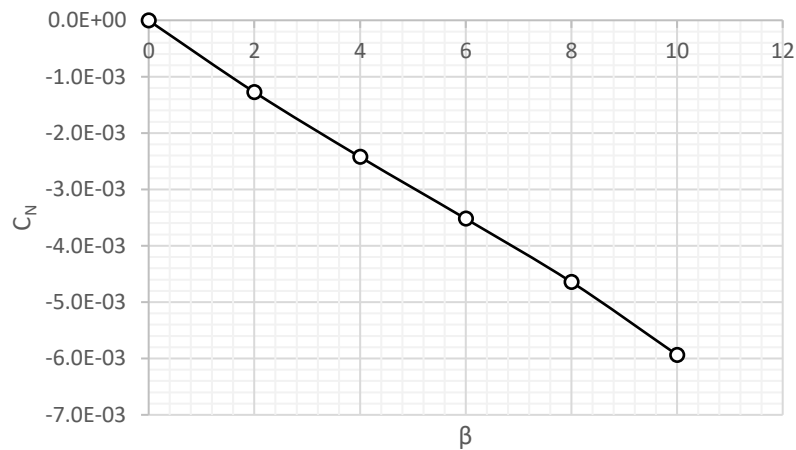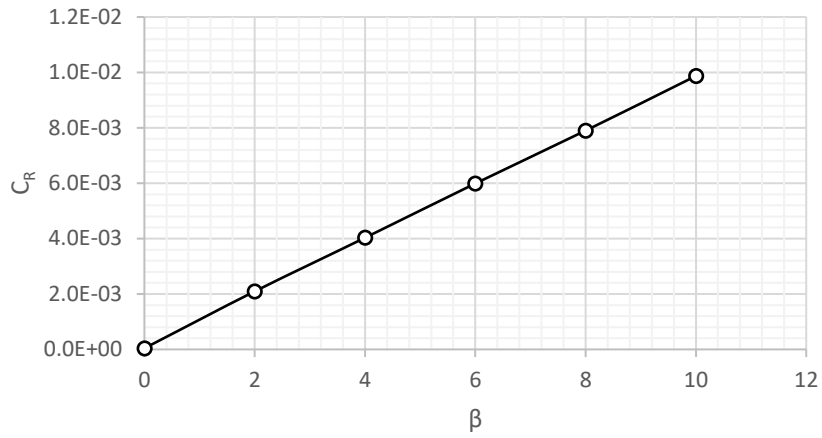
Figure 5.1 Lateral and directional PD-1's response to different β

5.2 Ruddervators effects on lateral and directional aerodynamics

In this paragraph is dealt the influence of antisymmetric deflections of the *ruddervators* on lateral and directional motion (*ruddervators* working as a rudder).
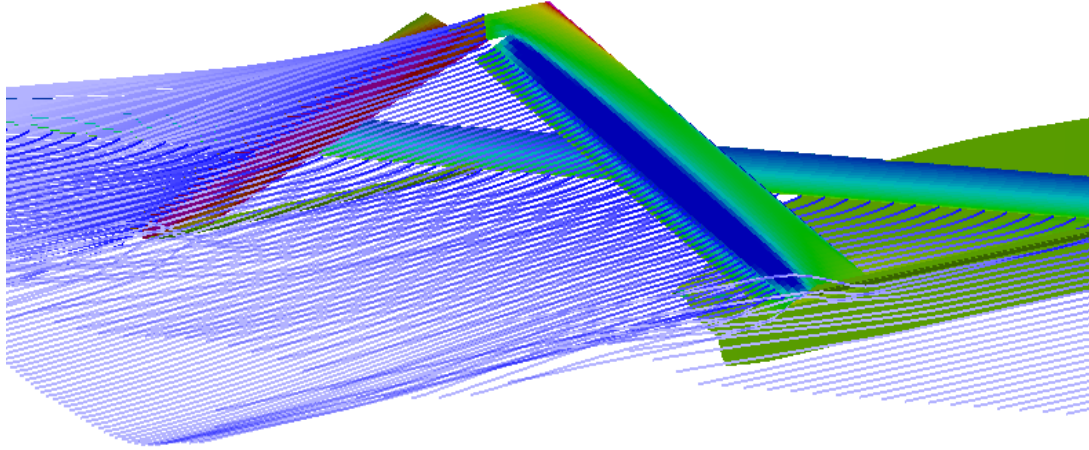
Figure 5.2 Ruddervators deflected asymmetrically with $\delta_r=30^\bullet$

As known lateral and directional motions are coupled rather than the longitudinal one that is analyzable alone. This brings lateral and directional control surfaces to affect both rolling and yawing moments.

Figure 5.3 and Figure 5.4 illustrate this statement, in fact we can observe that:

- The main target of *ruddervators* is creating a force behind CG normal to XZ plane that creates a yawing moment.
- *Ruddervators* creates an antisymmetric tailplane loading that provoke an undesired rolling moment too.
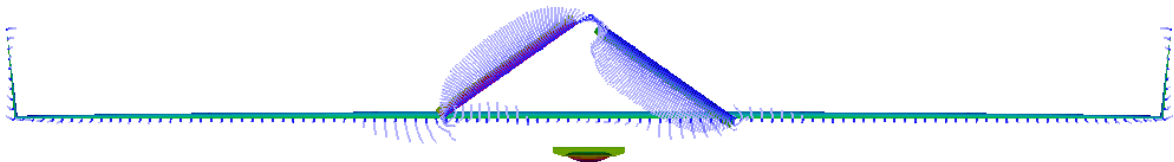
Figure 5.3 backview of ruddervators deflected asymmetrically with $\delta_r=30^\bullet$
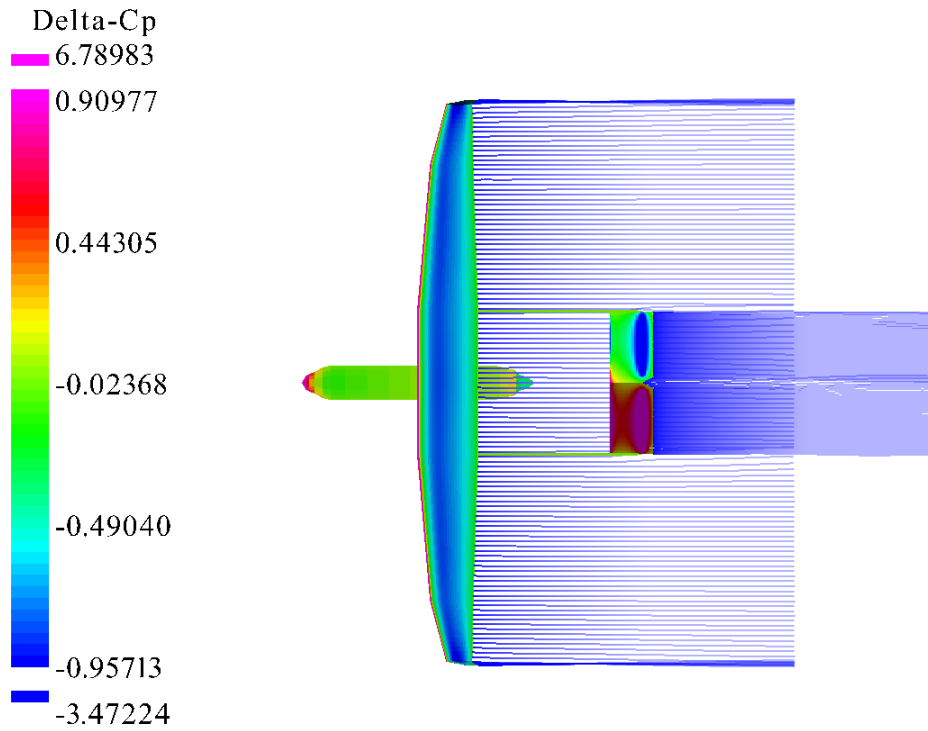
Figure 5.4 topview of ruddervators deflected asymmetrically with $\delta_r=30^\bullet$

5.2.1 Rolling Moment

This sub-section displays undesired effects of rudder on rolling moment:

β	$C_{R,\delta r=0°}$	$C_{R,\delta r=10°}$	$C_{R,\delta r=20°}$	$C_{R,\delta r=30°}$
0	4.1×10^{-5}	1.4×10^{-3}	2.7×10^{-3}	3.6×10^{-3}
2	2.1×10^{-3}	3.5×10^{-3}	4.7×10^{-3}	5.6×10^{-3}
4	4.0×10^{-3}	5.4×10^{-3}	6.7×10^{-3}	7.6×10^{-3}
6	6.0×10^{-3}	7.4×10^{-3}	8.6×10^{-3}	9.6×10^{-3}
8	7.9×10^{-3}	9.3×10^{-3}	1.1×10^{-2}	1.2×10^{-2}
10	9.9×10^{-3}	1.1×10^{-2}	1.3×10^{-2}	1.4×10^{-2}

Table 5.2 Undesired effect of the rudder on rolling moment
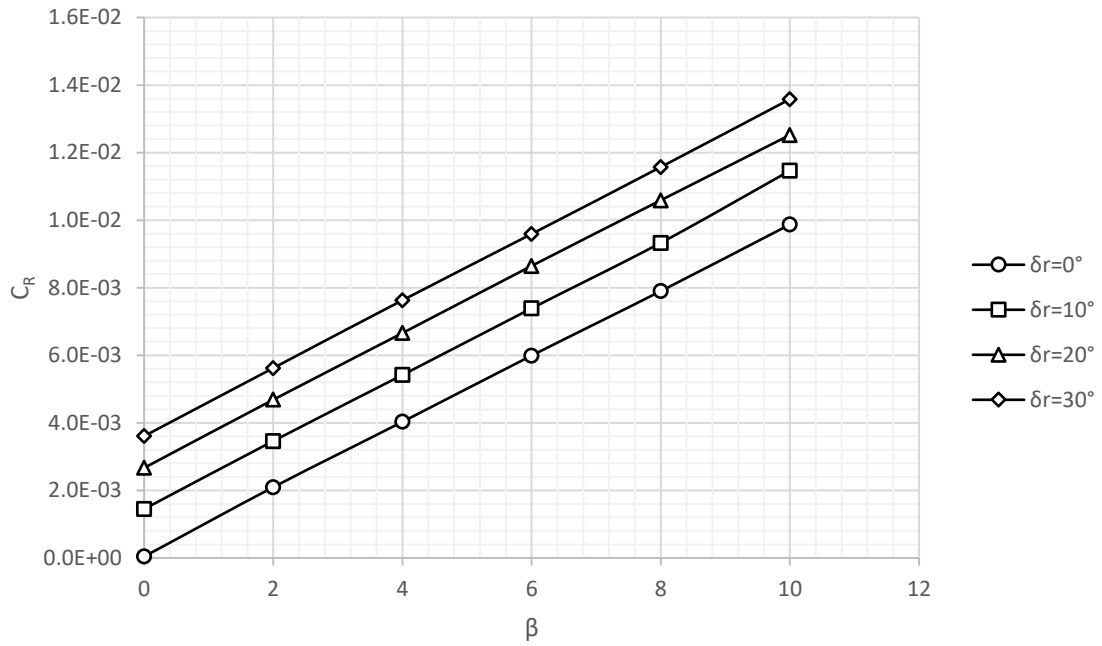
Figure 5.5 C_R vs δ_r

From this chart we can note that:

- with positive rudder's deflections C_R is positive even at β=0 (the curves are translating upward).
- The slopes of the lines are the same.

About the first point, it can be interesting to estimate the undesired control power $C_{R\delta r}$:

$$C_{R\delta r} = 1.4 \times 10^{-4} \ \text{deg}^{-1} \tag{5.1}$$

5.2.2 Yawing Moment

Now we will discuss about how rudder directly control directional stability. The data obtained with VSPAERO are contained in the Table below:

β	$C_{N,\delta r=0°}$	$C_{N,\delta r=10°}$	$C_{N,\delta r=20°}$	$C_{N,\delta r=30°}$
0	-3.9×10^{-6}	1.2×10^{-2}	2.1×10^{-2}	2.8×10^{-2}
2	-1.3×10^{-3}	9.7×10^{-3}	1.9×10^{-2}	2.7×10^{-2}
4	-2.4×10^{-3}	8.5×10^{-3}	1.8×10^{-2}	2.6×10^{-2}
6	-3.5×10^{-3}	7.4×10^{-3}	1.7×10^{-2}	2.5×10^{-2}
8	-4.6×10^{-3}	6.3×10^{-3}	1.6×10^{-2}	2.3×10^{-2}
10	-5.9×10^{-3}	4.9×10^{-2}	1.4×10^{-2}	2.2×10^{-2}

Table 5.3 effect of the rudder on yawing moment
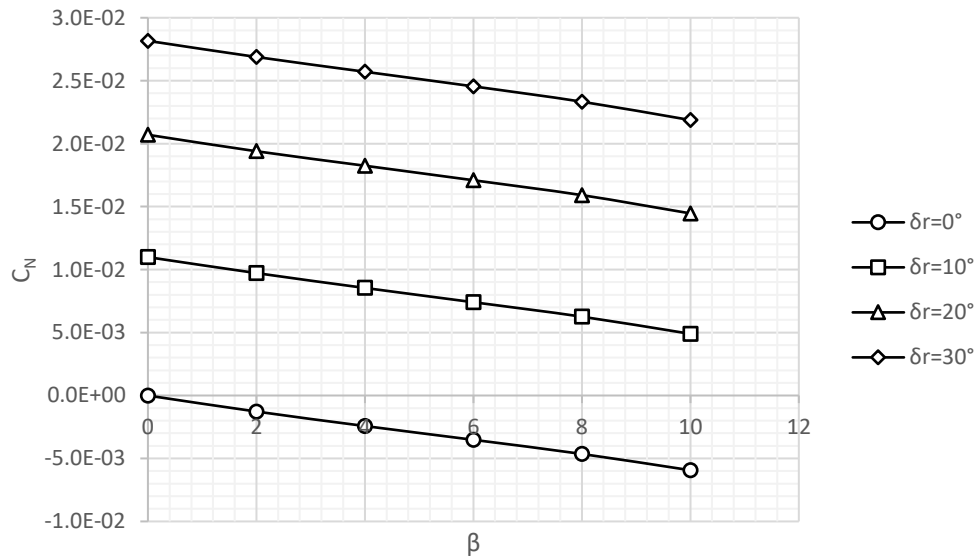
Figure 5.6 C_N vs δ_r

From this chart we can note that rudder alter C_N at the same way it does with C_R. Estimating the control power we obtain:

$$C_{N\delta r} = 1.10 \times 10^{-3} \text{ deg}^{-1} \tag{5.2}$$

Note how the direct control power is almost ten times larger than the undesired one.

5.2.3 Siderforce

β	$C_{Y,\delta r=0°}$	$C_{Y,\delta r=10°}$	$C_{Y,\delta r=20°}$	$C_{Y,\delta r=30°}$
0	-1.94×10^{-5}	0.036	0.067	0.091
2	-0.014	0.022	0.054	0.078
4	-0.027	0.009	0.040	0.065
6	-0.040	-0.004	0.027	0.052
8	-0.052	-0.017	0.014	0.038
10	-0.065	-0.029	0.002	0.026

Table 5.4 Effect of the rudder on sideforce
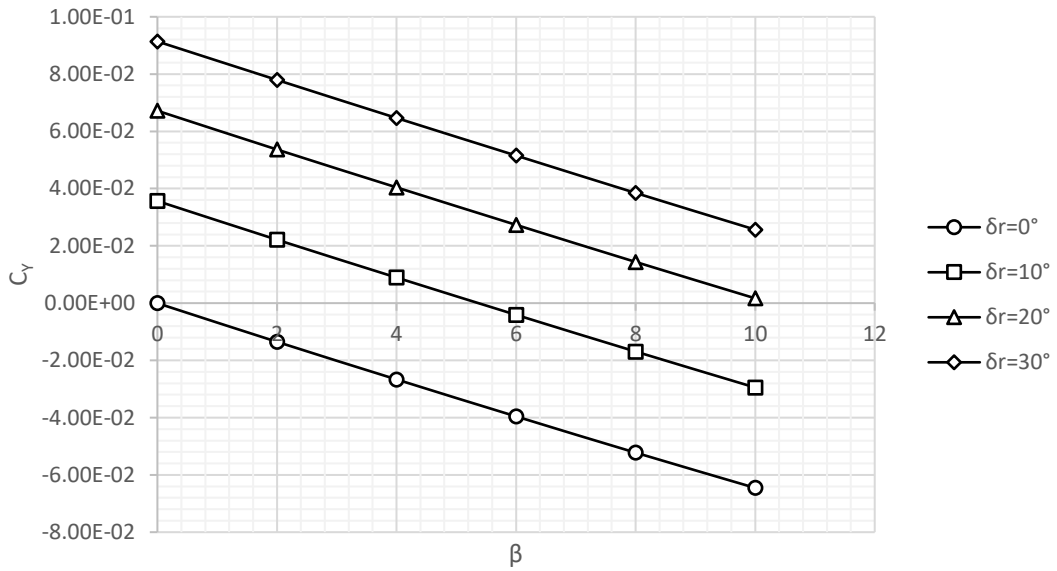
Figure 5.7 C_Y vs δ_r

Also in this case, the rudder deflections move upward the lines without changing their slope.

5.3 Ailerons effects on lateral and directional aerodynamics

Ailerons are the surfaces that directly control rolling moment. They do this by altering aircraft's wing loading as shown in Figure 5.8 and Figure 5.9. The latter shows even how trailing wakes are altered by the action of the control surfaces. Different lift produced by right and left wing bring to a moment around X axis (roll).

Ailerons, modifying lift, changes induced drag of the wing too. For example, watching Figure 5.8 we can note how the right wing creates more lift and then more induced drag than the left wing. This means that non-balanced drag forces produce an undesired moment around the Z axis (yaw).
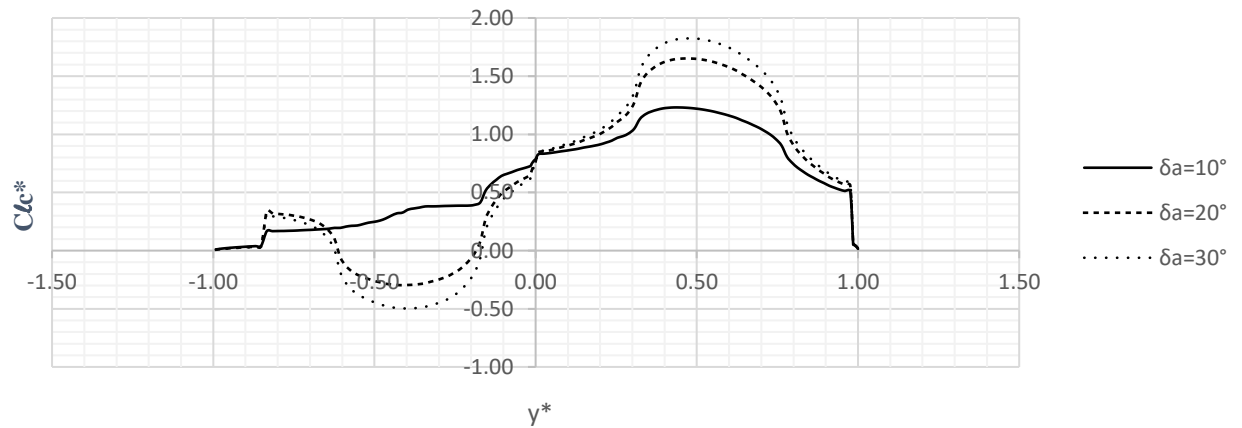
Figure 5.8 Wing loading at different δ_a
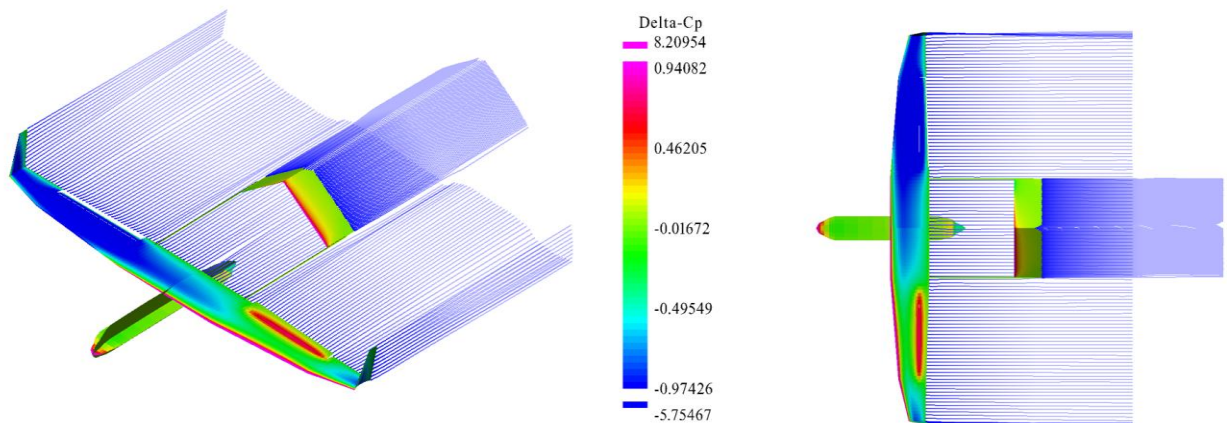
Figure 5.9 viewer lunched at $\delta_a=20°$

5.3.1 Rolling Moment

The results worked out by VSPAERO about ailerons' control power are contained in Table 5.5 and are viewable on the chart of Figure 5.10.

β	$C_{R,\delta r=0°}$	$C_{R,\delta r=10°}$	$C_{R,\delta r=20°}$	$C_{R,\delta r=30°}$
0	4.1×10^{-5}	0.050	0.095	0.114
2	0.002	0.052	0.097	0.115
4	0.004	0.054	0.098	0.114
6	0.006	0.056	0.100	0.118
8	0.008	0.057	0.101	0.120
10	0.010	0.059	0.102	0.119

Table 5.5 effect of ailerons on rolling moment
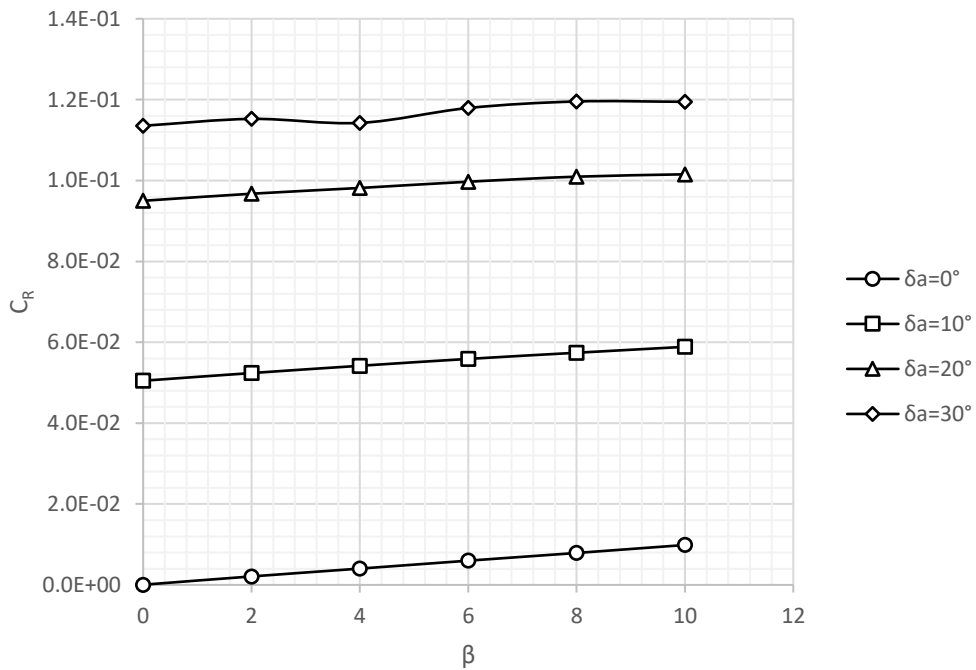
Figure 5.10 C_R vs δ_a

The deflections translate the lines upward thus C_{R0} increase its values when ailerons are deflected.

The estimated control derivative of ailerons is:

$$C_{R\delta a} = 5.05 \times 10^{-3} \text{ deg}^{-1} \tag{5.3}$$

5.3.2 Yawing Moment

As regards the undesired yawing moment, since VSPAERO shows numerical errors computing yaw coefficient at high ailerons deflection, we will show only two curves at δa=0° and δa=10°.

β	$C_{R,δa=0°}$	$C_{R,δa=10°}$
0	4.1×10^{-5}	0.050
2	0.002	0.052
4	0.004	0.054
6	0.006	0.056
8	0.008	0.057
10	0.010	0.059

Table 5.6 Undesired effect of ailerons on yawing moment
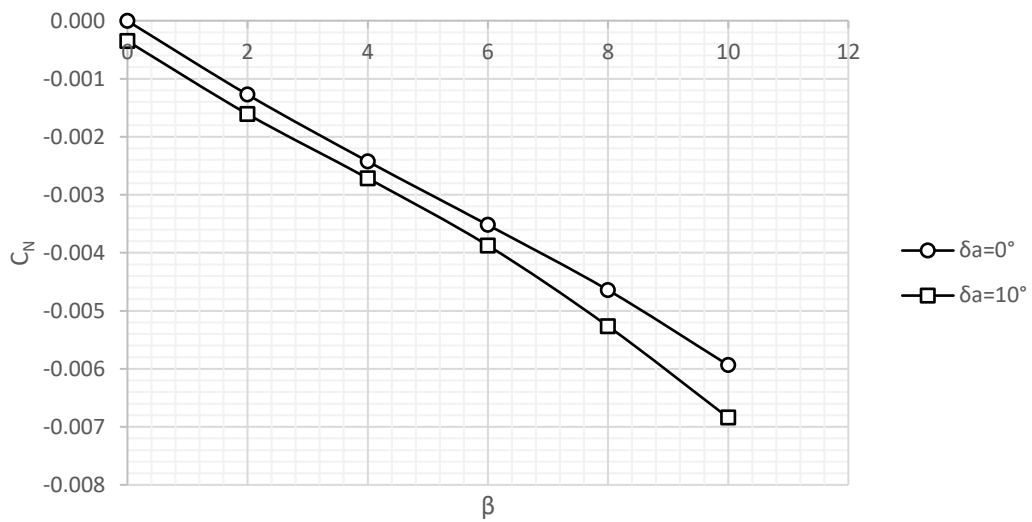
Figure 5.11 C_N vs $δ_a$

The estimated value of the undesired control power is:

$$C_{Nδa} = 3.49 \times 10^{-5} \text{ deg}^{-1} \tag{5.4}$$

Even in this case the direct control power is about ten times higher than the undesired one.

5.3.3 Siderforce

As regards sideforce:

β	$C_{Y,\delta a=0°}$	$C_{Y,\delta a=10°}$	$C_{Y,\delta a=20°}$	$C_{Y,\delta a=30°}$
0	-1.94×10^{-5}	0.003	0.005	0.006
2	-0.014	-0.011	-0.008	-0.007
4	-0.027	-0.024	-0.021	-0.020
6	-0.040	-0.037	-0.035	-0.035
8	-0.052	-0.050	-0.049	-0.048
10	-0.065	-0.063	-0.063	-0.063

Table 5.7 Effect of ailerons on sideforece
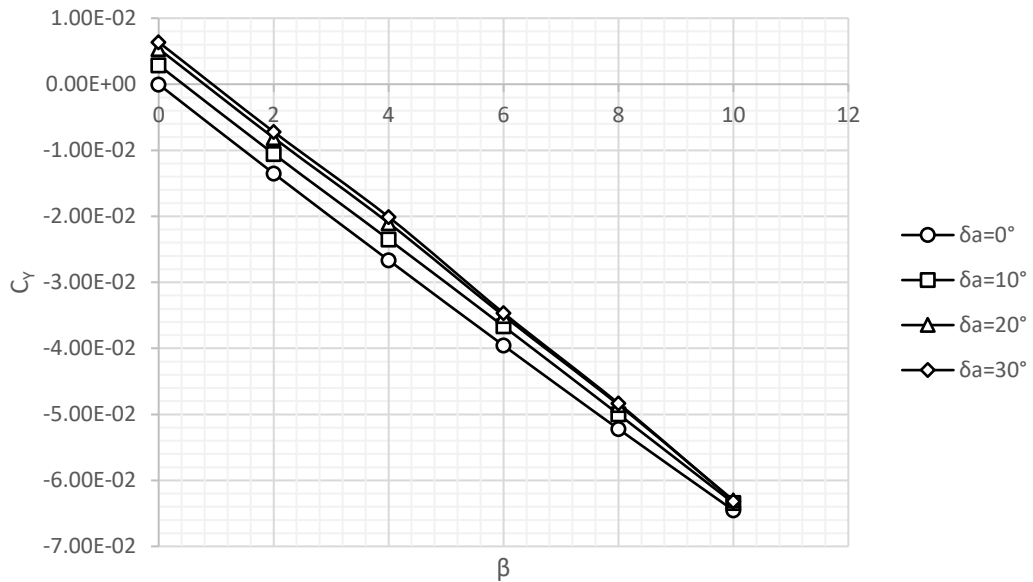
Figure 5.12 C_Y vs δ_a

5.4 Lateral and directional derivatives

The STABfile obtained running VSPAERO in steady mode contains other derivatives that we have not dealt in the previous chapter. These are summarized in Table 5.8:

/	∂C_R	∂C_N
$\partial\beta$	$1.02\text{x}10^{-3}$	$-5.95\text{x}10^{-4}$
∂p	$7.93\text{x}10^{-3}$	$-1.94\text{x}10^{-3}$
∂r	$-1.94\text{x}10^{-3}$	$-7.85\text{x}10^{-4}$
$\partial\delta r$	**$-1.46\text{x}10^{-6}$**	**$6.1\text{x}10^{-8}$**
$\partial\delta a$	**$5.15\text{x}10^{-3}$**	**$-4.07\text{x}10^{-5}$**

Table 5.8 Stability and control derivatives for lateral and directional motions

The values in bold have been already estimated and they are expressed in Equation 5.1, 5.2, 5.3 and 5.4. Comparing them it is possible to display the differences in the table below:

item	STABfile	ESTIMATES	difference %
$C_{R\delta r}$	$-1.46\text{x}10^{-6}$	$1.4\text{x}10^{-4}$	9762
$C_{N\delta r}$	$6.1\text{x}10^{-8}$	$1.10\text{x}10^{-3}$	1799500
$C_{R\delta a}$	$5.15\text{x}10^{-3}$	$5.05\ \text{x}10^{-3}$	2
$C_{N\delta a}$	$-1.46\text{x}10^{-6}$	$-3.49\text{x}10^{-5}$	14

Table 5.9 comparisons of longitudinal derivatives

Note how derivatives estimated in longitudinal aerodynamics were more accurate than these one and in particular how estimated rudder control power are completely imprecise.

6. Propulsive effects

6.1 Theoretical aspects and VSPAERO settings

PD-1's propeller is pushing and placed in the aircraft aft fuselage. As stated in Chapter 3, the propeller has been modelled as an actuator disk in VSPAERO calculations to estimate propulsive effects. What this chapter wants to study is how the aerodynamics of the aircraft is affected by the presence of the actuator disk. In fact, propulsive forces generated by the pressure jump through the disk can alter aircraft stability properties analyzed in the previous chapter. The main viewable effects are:

- Non-barycentric trust
- Changes of the tailplane loading

The latter is not so evident if studied with VSPAERO, in fact, the disk affects sections' wing loading only at its third/fourth decimal. Knowing this, what we expect are alterations that are more consistent in pitching moment than in lift.

From Figure 6.1 the actuator disk effects are visible on pressure distribution.
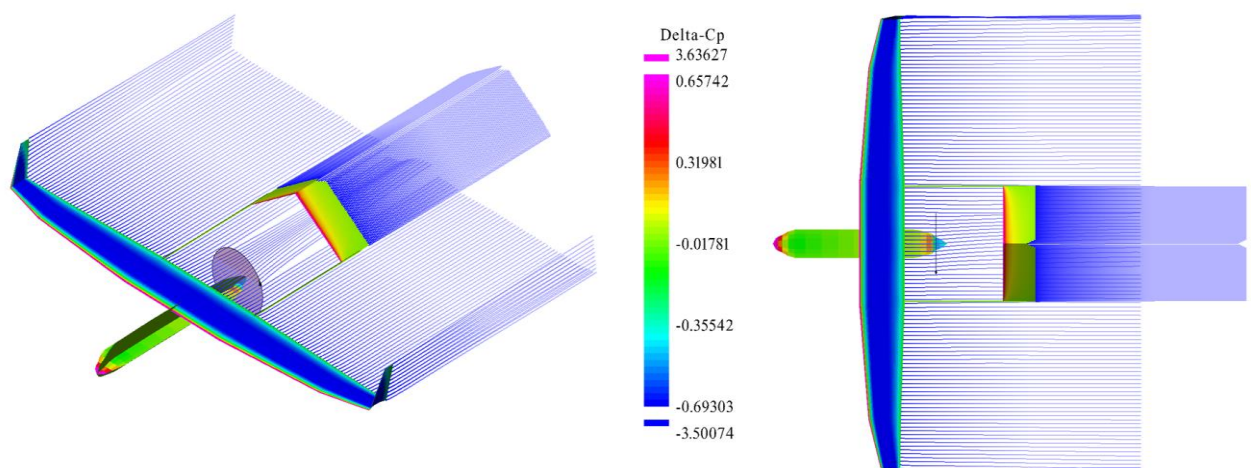
Figure 6.1 propulsive effects on the viewer

To calculate propulsive effects on VSPAERO the user must select on the advanced browser the desired propeller representation:

Figure 6.2 Prop representation choice

Then the software requires some propulsive parameters in the section "disk" of VSPAERO browser:
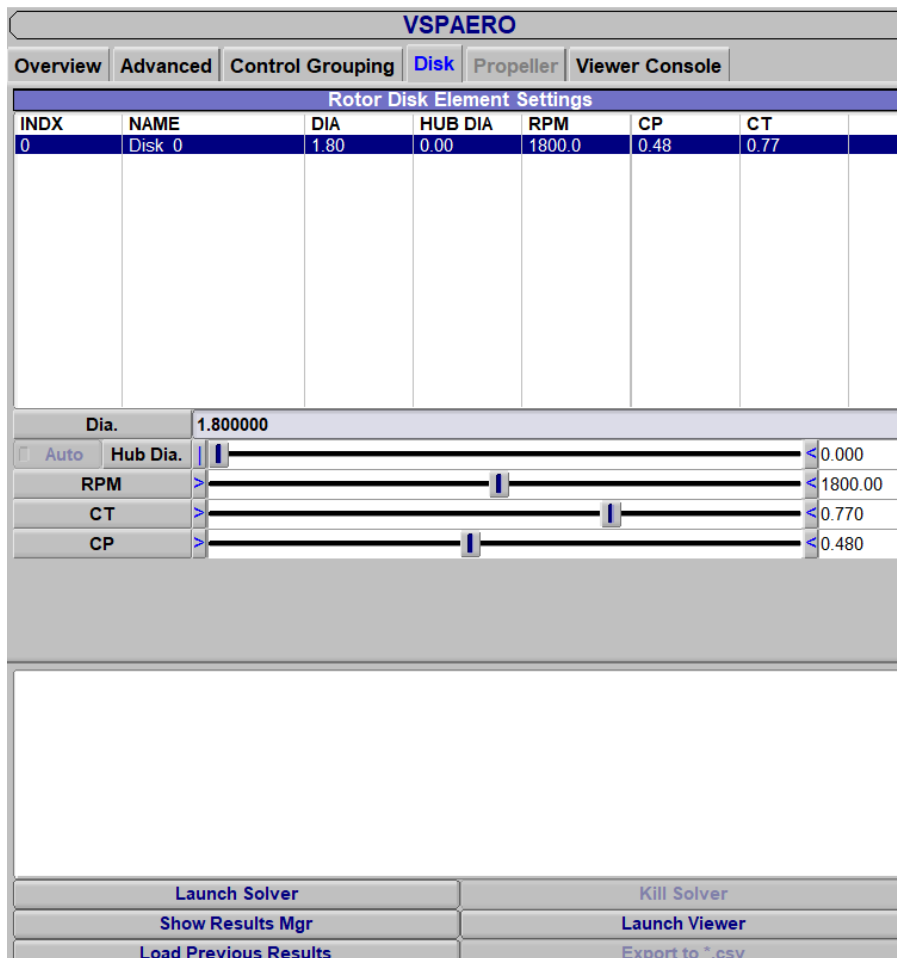
Figure 6.3 Disk settings

Note from Figure 6.3 that in the browser next to "disk" there is "propeller" that is grayed. When the user selects a prop representation only one of the two sections can be opened and edited.

The parameters in Figure 6.3 have been chosen considering a flight condition of surveillance at V_{FC}=21m/s and h_{FC}=3000m. Furthermore, they have been defined knowing the following input data:

ITEM	VALUE
P_{ax} (W)	3430
η_P	0.8
e	0.85
C_{LS}	1.50
C_{D0}	0.45
$C_{L,FC}$	1.35

Table 6.1 input parameters to evaluate disk settings

where the ones in italic have been estimated. Working on this data:

$$C_{D,FC} = C_{D0} + \frac{C_{L,FC}^2}{\pi ARe} = 0.1069 \tag{6.1}$$

$$T_{req,FC} = \frac{1}{2}\rho v^2 S C_{D,FC} = 31.1 \ N \tag{6.2}$$

$$P_{av,FC} = P_{ax}\eta_p = 2774 \ W \tag{6.3}$$

$$P_{req,FC} = T_{req,FC}V_{FC} = 652 \ W \tag{6.4}$$

$$T_{av,FC} = P_{av,FC}V_{FC} = 130.7 \ N \tag{6.5}$$

Made this calculation let's see how we choose the parameters D, C_T, C_P and RPM on disk settings (Figure 6.3):

D is the disk diameter

- RPM=1800 stems from that 61 CC 2-cylinder 4-stroke engine (PD-1's engine) has a working RPM range between 1500 and 7400 RPM and that we considered RPM and power as proportional.

- Trust coefficient: $C_T = \frac{T_{req,FC}}{\rho n^2 D^4} = 0.77$ (knowing that D is the disk diameter and $n = \frac{RPM}{60}$).

- Power coefficient: $C_P = \frac{P_{req,FC}}{\rho n^3 D^5} = 0.48$.

6.2 Propulsive effects on aerodynamic curves

6.2.1 Lift

α	$C_{L,\text{prop-off}}$	$C_{L,\text{prop-on}}$
0	0.52	0.52
2	0.71	0.71
4	0.90	0.90
6	1.10	1.09
8	1.29	1.28
10	1.47	1.47

Table 6.2 Prop effects on lift coefficient
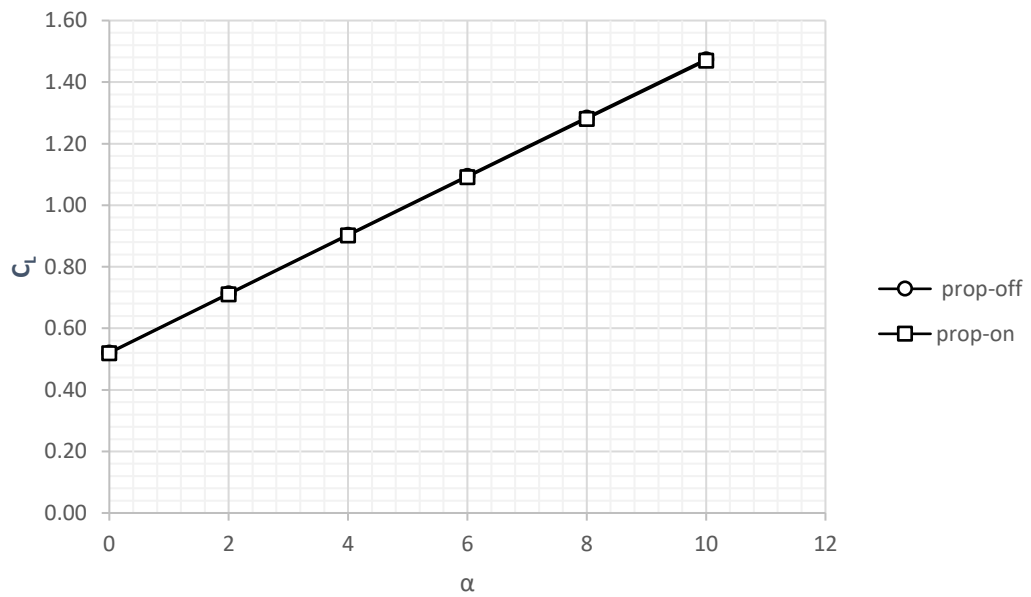
Figure 6.4 Prop effects on lift coefficient

As predicted, lift is not altered by propulsive effect.

6.2.2 Pitching moment

α	$C_{M,prop-off}$	$C_{M,prop-on}$
0	-0.093	-0.092
2	-0.158	-0.156
4	-0.225	-0.223
6	-0.295	-0.293
8	-0.368	-0.365
10	-0.444	-0.441

Table 6.3 Prop effects on pitching moment
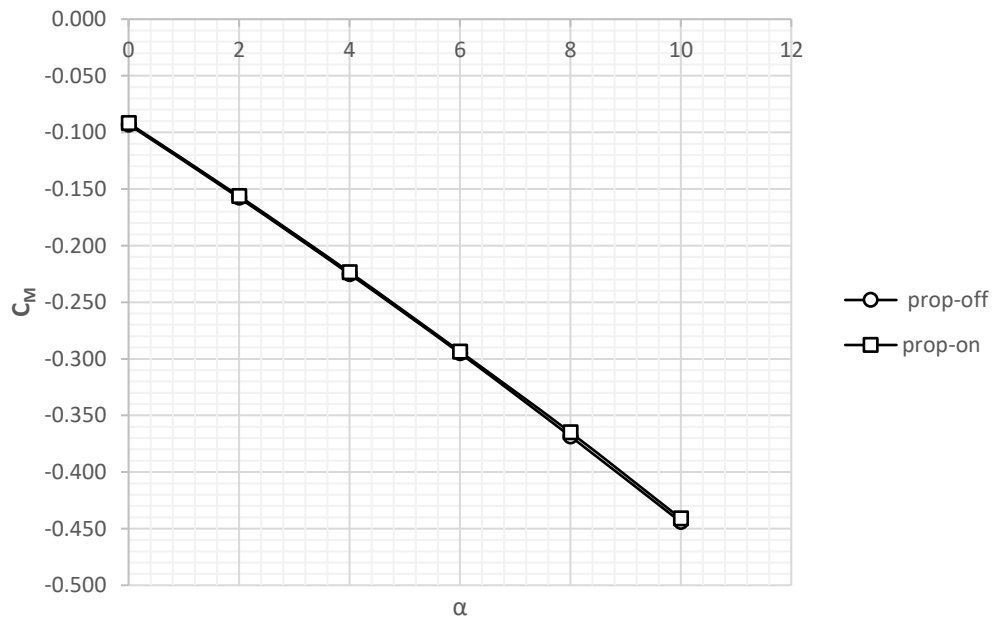
Figure 6.5 Prop effects on pitching moment

As regards the pitching moment, despite a little larger influence, propulsive effects are still negligible.

6.2.3 Drag and aerodynamic efficiency

α	$C_{D,prop-off}$	$C_{D,prop-on}$
0	0.023	0.021
2	0.031	0.029
4	0.041	0.039
6	0.054	0.052
8	0.069	0.067
10	0.086	0.085

Table 6.4 Prop effects on drag
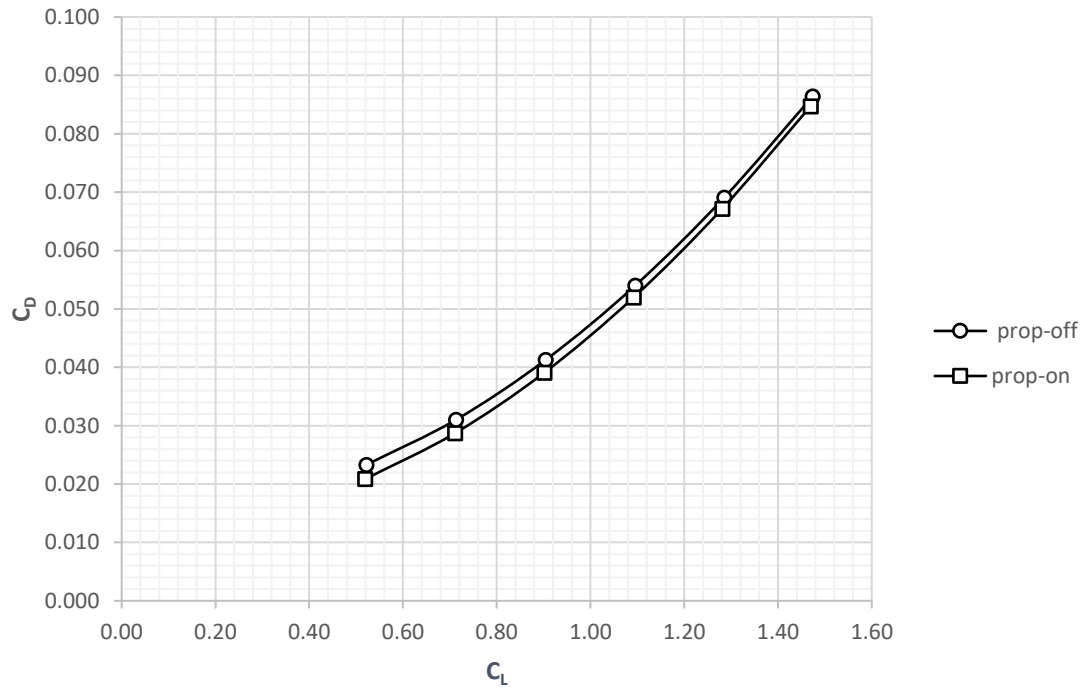
Figure 6.6 Prop effects on polar drag

α	$E_{prop\text{-}off}$	$E_{prop\text{-}on}$
0	22.40	24.90
2	22.99	24.76
4	21.91	23.06
6	20.29	21.02
8	18.61	19.07
10	17.06	17.35

Table 6.5 Prop effects on aerodynamic efficiency
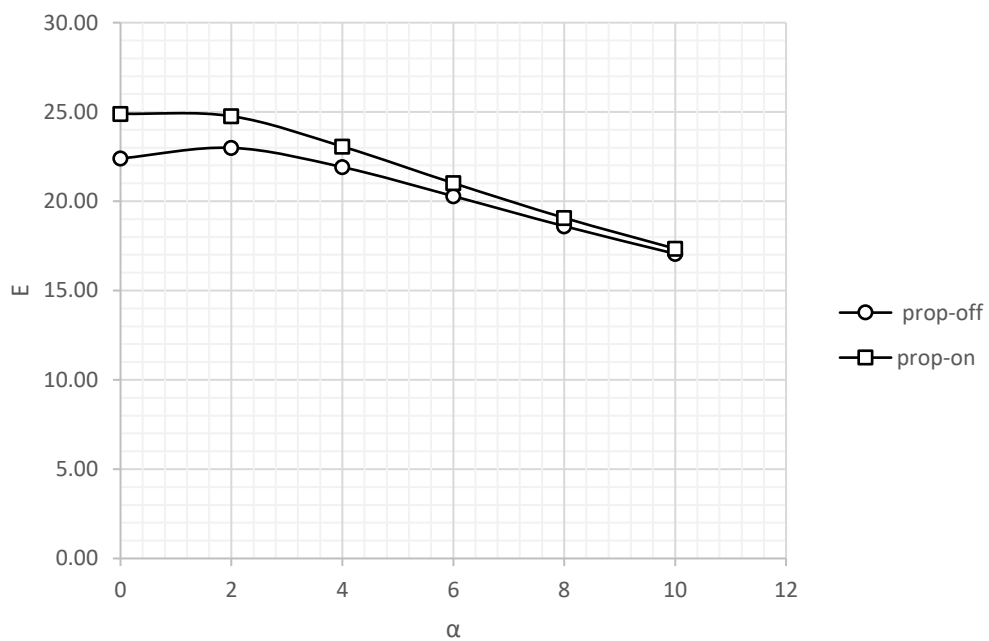
Figure 6.7 Prop effects on aerodynamic efficiency

Propulsive effects are more relevant on drag and aerodynamic efficiency. In particular, the disk unexpectedly reduces drag and increases efficiency even in a consistent way as long as the aircraft flies at low α.

Remember that VSPAERO do not account for parasite drag, thus these observations are not completely reliable.

7. PD-1's Performance

In this chapter it will be shown an overall of the PD-1's performance. This study has been made with a pre-realized MATLAB script and it will complete this thesis work. The input data that the script requires are:

- Geometric
- Aerodynamic
- Propulsive

Geometry and weights are declared by the producer instead aerodynamic and propulsive data have been obtained from the previous analysis or they have been estimated. The script also needs flight conditions to be launched. In the following analysis there have been chosen a cruise altitude of 3000 m and climb altitude of 1500 m.

Input parameters are summarized in the table below:

item	value
S	1.4 m^2
b	4.0 m
C_{D0}	0.045
C_{Lmax}	1.50
e	0.85
C_{LmaxTO}	1.60
C_{LmaxL}	1.70
C_{Lg}	0.70
n_{max}	2.00
φ_{rev}	0.40
P_{ax}	4.6 hp
SFC	0.66 lb/(lb·h)
W_{TO}	40 kg
W_{fuel}	9 kg

Table 7.1 MATLAB script input paramters

7.1 Technical polar

Point	C_L	C_D	E	V	$D=T_{req}$	P_{req}
E	1.15	0.09	12.79	19.59 m/s	30.7 N	600.8 W
P	1.99	0.18	11.08	14.88 m/s	35.4 N	527.1 W
A	0.66	0.06	11.08	25.78 m/s	35.4 N	913.0 W
S	1.50	0.12	12.36	17.16 m/s	31.7 N	544.9 W

Table 7.2 Characteristic point data at sea level

Point	C_L	C_D	E	V	$D=T_{req}$	P_{req}
E	1.15	0.09	12.79	21.08 m/s	30.7 N	646.4 W
P	1.99	0.18	11.08	16.01 m/s	35.4 N	567.2 W
A	0.66	0.06	11.08	27.74 m/s	35.4 N	982.3 W
S	1.50	0.12	12.36	18.47 m/s	31.7 N	586.3 W

Table 7.3 Characteristic point data at climb altitude

Point	C_L	C_D	E	V	$D=T_{req}$	P_{req}
E	1.15	0.09	12.79	22.74 m/s	30.7 N	697.4 W
P	1.99	0.18	11.08	17.28 m/s	35.4 N	611.9 W
A	0.66	0.06	11.08	29.92 m/s	35.4 N	1059.8 W
S	1.50	0.12	12.36	19.92 m/s	31.7 N	632.5 W

Table 7.4 Characteristic point data at cruise altitude
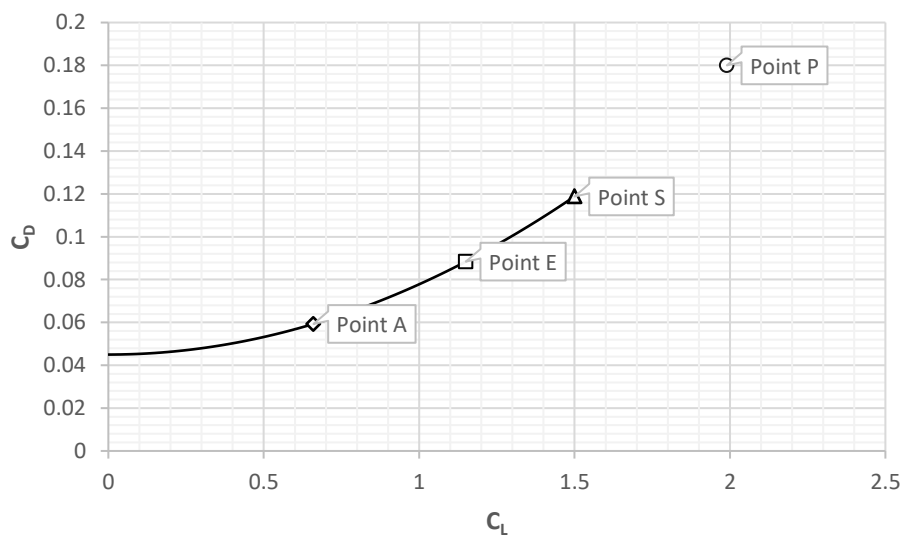
Figure 7.1 Drag polar
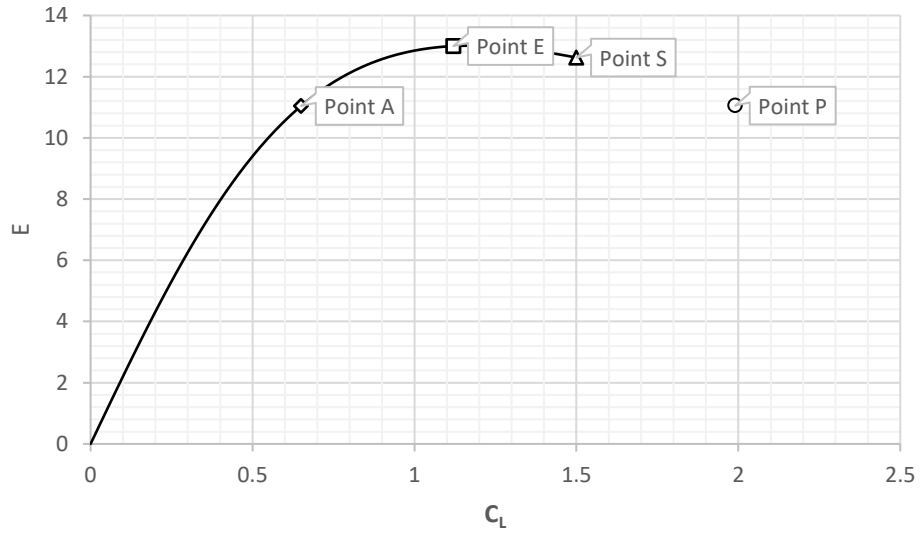
Figure 7.2 Lift-to-drag ratio vs lift coefficient

Since C_{LP} is higher than C_{LS}, the point P is only a theoretical point, i.e it describes a flight condition that is not achievable by the aircraft.
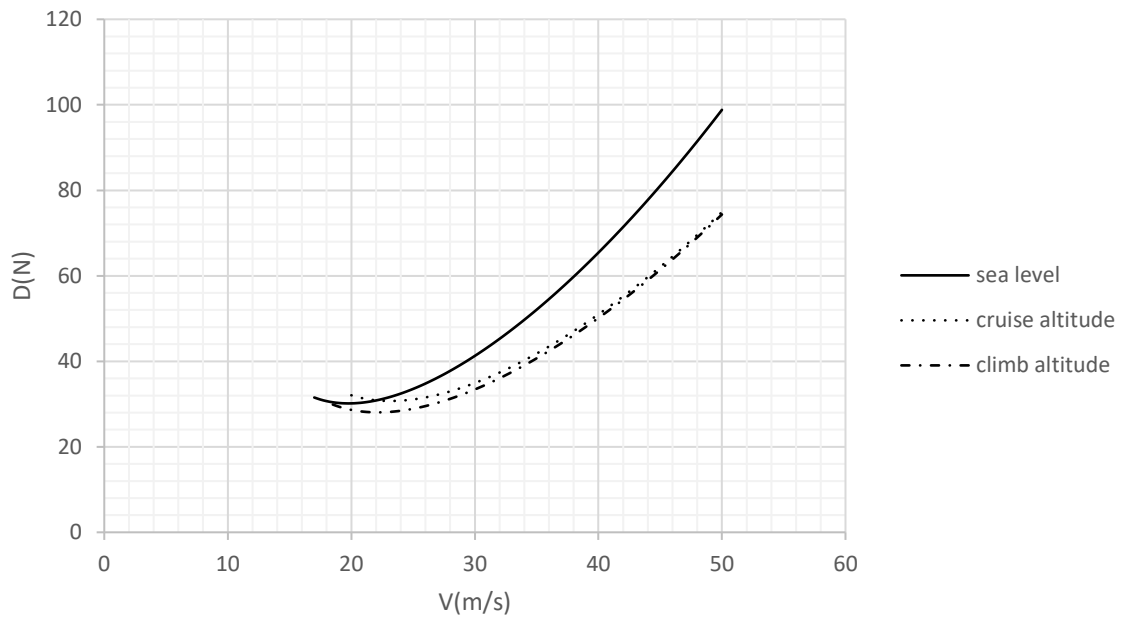
Figure 7.3 Required trust for level flight
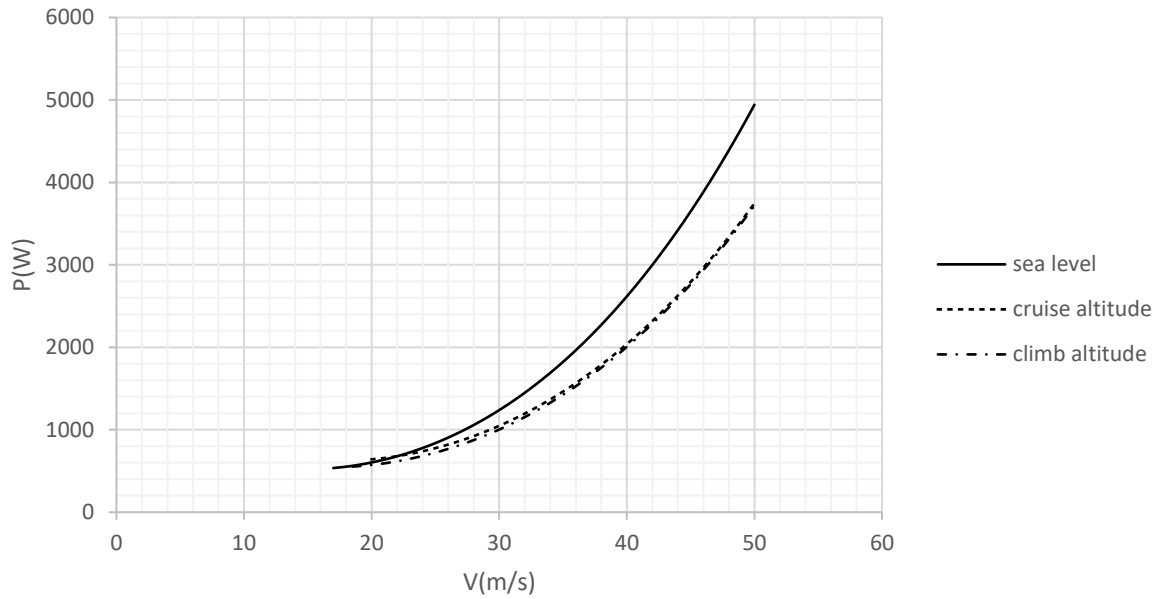
Figure 7.4 Required power for level flight

7.2 Propulsive performance

To value propulsive performance, it is necessary to select some other parameters. We will choose $V_{FC}=22$ m/s and a throttle $\varphi=1.00$ to value maximum trust and power available. Furthermore, to estimate fuel consumes it has been considered a flight time of 7 hours.

item	Value (metric)	Value (imperial)
T	92.75 N	2.12 lbf
P	2037 W	2.7 hp
Fuel consumption	7.15 Kg	15.77 lb

Table 7.5 Max propulsive performance and consume at V_E

7.3 Climb and ceiling

As regards climbing performance, note that the maximum rate of climb for propeller aircraft is achievable for $V \approx V_P$. Point P cannot be obtained as observed in the previous chapter thus in the following table are presented maximum theoretical RC (at h=0m and h=3000m) and RC obtained at $V=V_{FC}$. Obviously, every values have been computed for $\varphi=1.00$.

Item	V_{TAS}	RC	θ_{RC}
$RC_{MAX(h=0)}$	14.88 m/s	5.65 m/s	21.8°
$RC_{MAX(h=3000)}$	17.3 m/s	3.63 m/s	12°
$RC_{h=3000}$	22 m/s	3.5 m/s	9°

Table 7.6 climbing performance

Climb flight time to reach cruise altitude is shown below. The script computes this value in point P conditions thus it is an ideal time.

$$T_{min} = 657 \ s \tag{7.1}$$

item	value
Absolute ceiling (RC=0)	8468 m
Service ceiling (RC=0.5)	7711 m

Table 7.7 Absolute and service ceilings

7.4 Level Flight

To obtain the maximum speed at cruise condition, the script lets the user choose a throttle (it has been selected φ=1.00) and then it calculates the speed using both an analytic approach and a graphic one. The latter is based on the comparison between requested and available power considering altitude and throttle (Figure 7.5).
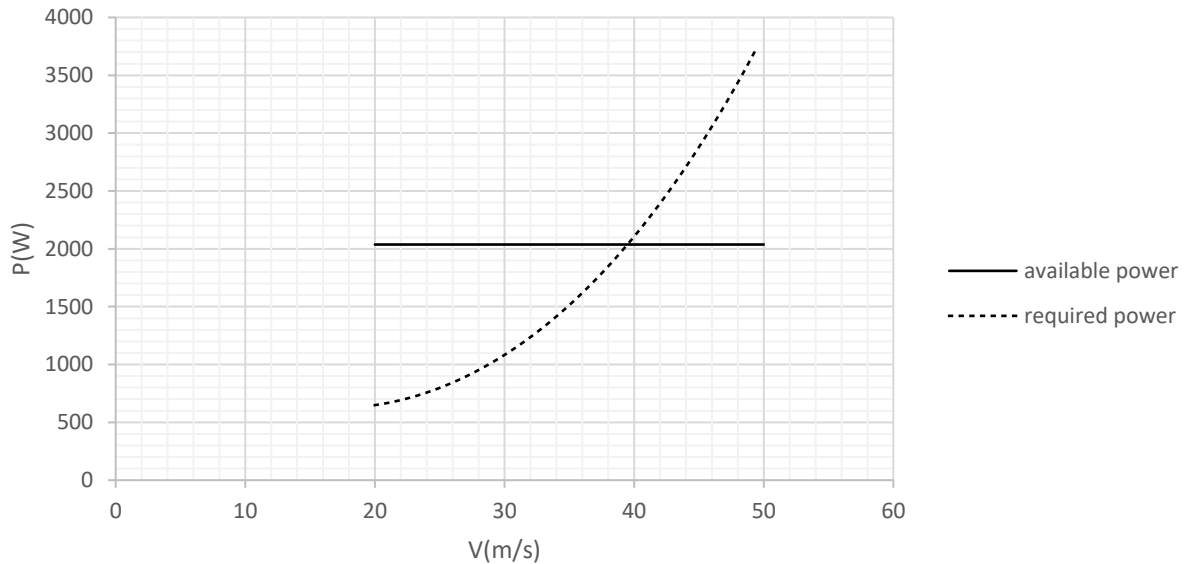
Figure 7.5 comparison between available and requested power at a cruise altitude of 3000m.

Changing the throttle, the available power line moves up and down and then even the intersection point between the two curves moves. It is easy to note that the intersection point cannot be more to the right than at φ=1.

The results of both analyses are shown in the table below:

item	value
$V_{MAX\,(graphic)}$	39.5 m/s
$V_{MAX\,(analtic)}$	39.6 m/s

Table 7.8 maximum speed

7.5 Autonomies

For this calculation, the script uses point P conditions as reference for maximum endurance and point E as reference for maximum range but, it calculates range and autonomies also at the selected V_{FC}. The calculations are realised both at fixed speed and at fixed altitude.

item	value
En_{max}	35.89 hr
R_{max}	2416 km

Table 7.9 max autonomies at fixed altitude

item	value
En_{max}	33.66 hr
R_{max}	2416 km

Table 7.10 max autonomies at fixed speed

item	value
En	32.47 hr
R_{max}	2411 km
V_{fin}	19.34 m/s

Table 7.11 autonomies at $V_{in}=V_{FC}$ and fixed altitude

item	value
En	30.44 hr
R_{max}	2411 km
h_{fin}	3532 m

Table 7.12 autonomies at fixed speed

Note how range is independent from altitude for propeller aircraft.

7.6 Take-off And Landing

item	value
S_{TO}	134m
S_L	323m

Table 7.13 take-off and landing distances at temperature of 15°C

7.7 Turn

Selecting a load factor n=1.2 and V=V_{FC}, these are the results:

item	value
R	74.4 m
ω	16.9 deg/s
φ	33.6°

Table 7.14 Turn performance

In the table below are summarized the best sustainable parameters:

item	value
V_{min}	29.4 m/s
R_{min}	45.5 m
ω_{max}	37 deg/s
φ_{max}	62.7°
n_{max}	2.18

Table 7.15 Max sustainable parameters

Conclusion

This thesis has shown how using OpenVSP and VSPAERO is possible to perform a complete aerodynamic analysis of an aircraft. As it has been pointed out during the work, VSPAERO is not able to evaluate some aerodynamic phenomena, but this software's aim is not to realise completely reliable aerodynamic studies rather make them quick and simple. An interesting development of this work can be the comparison between these results and the ones obtained from an advanced CFD simulation other than the check with wind tunnel tests.

Bibliography

[1] Advanced UAV aerodynamics, Flight stability and control, Pascual Marqués, Andrea Da Ronch John Wiley & Sons, Apr 27,2017.

[2] Unmanned Aircraft Systems: UAVS Design, Development and Deployment, Reg Austin, John Wiley & Sons, Sep 20, 2011

[3] Software Testing: VSPAERO, Floris Mariën, Prof. Dr.-Ing. Dieter Scholtz, 16/07/2021

[4] Aerodynamic analysis and surrogate modelling of distribuited propulsion on commuter and regional aircraft through VLM and CFD methods, Biagio Ambrosino, Luca De Martino, Prof. Pierluigi Della Vecchia, Prof Agostino De Marco, A.A 2018/2019

[5] Geometric modelling and static stability analysis of the Canadair water bomber with JPAD and OpenVSP, Salvatore Trepiccione, Danilo Ciliberti, A.A 2021/2022

[6] OpenVSP website: http://openvsp.org

[7] Airfoil Tools website: http://airfoiltools.com